

PHOTOMETRIC REVERBERATION MAPPING OF THE BROAD EMISSION LINE REGION IN QUASARS

DORON CHELOUCHE¹ AND ELIRAN DANIEL²

Draft version January 25, 2013

ABSTRACT

A method is proposed for measuring the size of the broad emission line region (BLR) in quasars using broadband photometric data. A feasibility study, based on numerical simulations, points to the advantages and pitfalls associated with this approach. The method is applied to a subset of the Palomar-Green quasar sample for which independent BLR size measurements are available. An agreement is found between the results of the photometric method and the spectroscopic reverberation mapping technique. Implications for the measurement of BLR sizes and black hole masses for numerous quasars in the era of large surveys are discussed.

Subject headings: galaxies: active — methods: data analysis — quasars: emission lines — surveys — techniques: photometric

1. INTRODUCTION

Black holes (BH) are physical entities that provide insight into the foundations of (quantum-) gravity theories. Such objects are characterized by three basic properties: mass, angular momentum, and charge. Among these properties the most fundamental is the mass, which characterizes all BHs. Angular momentum is only relevant for rotating (Kerr) BHs while charge is less relevant for astrophysical BHs.

Currently, the best evidence for the existence of BH is astrophysical. In particular, a broad range of BH masses is implied by astronomical observations: from solar mass BHs as the end products of massive stars to supermassive BHs (SMBH) at the centers of galaxies with masses that may easily exceed a million solar masses (Salpeter 1964; Lynden-Bell 1969).

Perhaps the first evidence for the presence of SMBH at the centers of galaxies is associated with quasars and other types of active galactic nuclei (to which we shall henceforth refer to, generally, as quasars). In those objects, gas from the medium surrounding the SMBH, that is able to lose angular momentum and spiral inwards, eventually accretes onto it. As the gas accretes, its gravitational energy is effectively converted to radiation with most of the emitted flux originating from the immediate vicinity of the SMBH, where the gas reaches the highest temperatures (Shakura & Sunyaev 1973).

The mass of SMBHs in small samples of low redshift non-active galaxies has been measured using, for example, maser- and stellar-kinematics (Miyoshi et al. 1995; Genzel et al. 1997; Gebhardt et al. 2000). For most low redshift galaxies, SMBH mass estimation is, however, indirect and involves scaling relations that were derived for small samples of objects for which direct mass measurements were possible (Magorrian et al. 1998).

As one attempts to estimate the mass of black holes at higher redshifts, various complications arise: it is not clear that locally determined scaling laws apply also to higher redshift objects since galaxies and their environments evolve with cosmic time. Furthermore, high redshift objects discovered by flux-limited samples are often much brighter than their low- z counterparts, and it is yet to be established whether ex-

trapolated relations are at all relevant in that regime (Netzer 2003). For these reasons, direct SMBH mass determination of intermediate- and high-redshift objects is the most reliable way to further our understanding of SMBH-galaxy formation and co-evolution, and to reach a reliable census of black holes in the universe.

Direct mass determination of SMBHs at high redshifts is currently limited to quasars, which are among the brightest objects in the universe and are powered by the SMBH itself. While quasars certainly trace the galaxy population, they also present a particular epoch in a galaxy lifetime, in which the black hole is accreting gas, and is at a stage of rapid growth. Therefore, better understanding of the SMBH demography in low- and high- z quasars has far-reaching implications for galaxy/black-hole formation and co-evolution (Ferrarese et al. 2001; Shields et al. 2003; Osmer 2004; Hopkins et al. 2006; Kollmeier et al. 2006; Shields et al. 2006; Greene & Ho 2006; Woo et al. 2008; Trakhtenbrot & Netzer 2010).

A reliable method to directly measure the mass of SMBHs in quasars involves the reverberation mapping of the broad emission line region (BLR) in those objects (Bahcall et al. 1972; Peterson 1993). This region is known to be photo-ionized by the central continuum source (Baldwin & Netzer 1978), and its emission, in the form of broad permitted emission lines, is seen to react to continuum variations. Studies have shown that the BLR lies at distances, R_{BLR} , that are much larger than the SMBH Schwarzschild radius, and also larger than the size of the continuum emitting region, i.e., the accretion disk. That being said, the BLR lies at small enough distances so that its kinematics is primarily set by the SMBH, which has a prominent contribution to the gravitational potential on those scales. That this is the case may be deduced from the velocity dispersion of the emitted gas, as inferred from the width of the broad emission lines, which is typically of order a few $\times 10^3 \text{ km s}^{-1}$, as well as from the fact that, in luminous quasars, line variations lag behind relatively rapid continuum variations with typical time delays, $t_{\text{lag}} \sim R_{\text{BLR}}/c \simeq 200$ days, where c is the speed of light (Kaspi et al. 2000, and references therein).

Technically, reverberation mapping involves multi-epoch spectroscopic observations so that continuum and emission line variations may be individually traced (Dietrich et al. 1993; Netzer & Peterson 1997; Kaspi et al. 2000). Contin-

¹ Department of Physics, Faculty of Natural Sciences, University of Haifa, Haifa 31905, Israel; doron@sci.haifa.ac.il

² Department of Physics, Technion, Haifa 32000, Israel; elirand-viv@gmail.com

uum and emission line light curves can then be used to infer the size of the broad emission line region using a cross-correlation analysis (Blandford & McKee 1982, and §2.2). By measuring R_{BLR} and the velocity dispersion of the gas (via spectral modeling of the emission line profile and by defining a measure of the velocity dispersion of the gas), the SMBH mass may be deduced, up to a geometrical factor of order unity (Peterson & Wandel 1999; Krolik 2001). Mass determinations using this technique have been shown to be consistent with the results of other independent methods (Gebhardt et al. 2000; Ferrarese et al. 2001; Peterson 2010), and are thought to be accurate to within 0.5 dex (Krolik 2001).

Nowadays, reverberation mapping has a central role in determining SMBH masses in active galaxies and for shedding light on the physics of the central engine in these objects³. Nevertheless, despite several decades of spectroscopic monitoring of quasars, reliable BLR sizes and corresponding SMBH mass measurements have been determined for only a few dozens of low- z objects (Gaskell & Sparke 1986; Koratkar & Gaskell 1991; Dietrich et al. 1993; Kaspi et al. 2000; Peterson et al. 2004; Kaspi et al. 2005; Peterson et al. 2005; Bentz et al. 2009; Peterson 2010; Barth et al. 2011). Using the results of reverberation mapping, various scaling relations were found and quantified including, for example, the R_{BLR} (or SMBH mass) vs. quasar luminosity relation (Koratkar & Gaskell 1991; Kaspi et al. 2000; Peterson et al. 2004; Kaspi et al. 2007; Bentz et al. 2009), the SMBH mass vs. the quasar’s optical spectral properties relation (Greene & Ho 2005), and the black hole-host galaxy bulge mass relation in quasars (Wandel 1999).

Despite being derived from small samples of nearby objects, the aforementioned relations are often extrapolated to reflect on the quasar population as a whole (Vestergaard 2002; Vestergaard & Osmer 2009), sometimes with little justification (Netzer 2003; Kaspi et al. 2007; McGill et al. 2008; Zhang et al. 2008). Potential biases arising from uncertain extrapolations to high redshifts, or to different sub-classes of quasars, may crucially affect our understanding of black hole growth and structure formation over cosmic time (Kauffmann & Haehnelt 2000; Netzer 2003; Collin & Kawaguchi 2004; Pelupessy et al. 2007; Trakhtenbrot & Netzer 2010). Clearly, an efficient way to implement the reverberation mapping technique is highly desirable as it would alleviate many of the uncertainties currently plaguing the field.

Motivated by upcoming photometric surveys that will cover a broad range of wavelengths and will regularly monitor a fair fraction of the sky with good photometric accuracy (e.g., the *Large Synoptic Survey Telescope*, LSST), we aim to provide proof-of-concept that photometric reverberation mapping of the BLR in quasars is feasible. In a nut shell, instead of spectrally separating line and continuum light curves from multi-epoch spectroscopic observations, we take advantage of the different variability properties of continuum and line processes and separate them at the light curve level. In this work we have no intention to address the full scope of issues associated with time-series analysis but rather hope to trigger further

³ It is worth noting that, in addition to SMBH mass measurement, the structure and geometry of the BLR may be probed by means of velocity-resolved reverberation mapping of the broad emission lines (Korista et al. 1995; Wanders et al. 1995; Kollatschny 2003; Bentz et al. 2010). Such investigations cannot be carried out using broadband photometric reverberation techniques, which do not resolve the emission lines, and will not be discussed here any further.

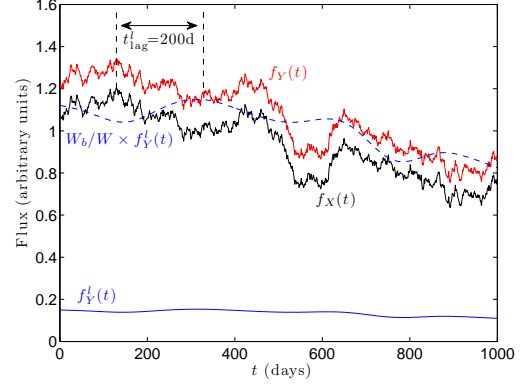


Figure 1. A realization of the broadband photometric light-curves of a typical quasar (see text). Flux variations in the X (black) and Y (red) bands show an overall similarity due to the large contribution of highly correlated continuum emission processes to both bands. The response of an emission line to continuum variations in the X-band is shown in dashed blue lines ($t_{\text{lag}} = 200$ days was assumed). The Y-band light-curve includes a 13% contribution to the total flux from a broad emission line (solid blue line). A case where the noise level is negligible ($\delta / \langle f \rangle = 10^{-3}$) was assumed for clarity. observational and theoretical work in broadband reverberation mapping of quasar BLRs.

This paper is organized as follows: section 2 presents the photometric approach to reverberation mapping using analytic means and by resorting to simulations of quasar light curves. The reliability of the photometric method for line-to-continuum time lag measurement is investigated by means of simulations in §3. In §4 we apply the method to a subset of the Palomar-Green (PG) quasar sample (Schmidt & Green 1983), for which previous measurements of the BLR size are available (Kaspi et al. 2000). Summary follows in §5.

2. THE FORMALISM

Here we present the algorithm for reverberation mapping the broad emission line regions in quasars using broadband photometric means. We first describe our model for quasar light curves (§2.1) and then analyze them using new statistical methods that are developed in §2.2.

2.1. A model for the light-curve of quasars

To demonstrate the feasibility of photometric reverberation mapping, we first resort to simulations. Specifically, we rely on current knowledge of the typical spectrum of quasars, and the variability properties of such objects, to construct a model for the light curves in different spectral bands.

2.1.1. Continuum emission

Quasar light-curves are reminiscent of red noise, following a power spectrum $P(\omega) \sim \omega^\alpha$ (ω is the angular frequency) with $\alpha \simeq -2$ (Giveon et al. 1999, and references therein). Here we model the pure continuum light-curve in some band X as a sum of discrete Fourier components, each with a random phase ϕ_i :

$$f_X^c(t) = \sum_{i=1}^{\infty} A(\omega_i) \sin(\omega_i t + \phi_i). \quad (1)$$

The amplitude of each Fourier mode, $A(\omega_i) \propto \omega_i^{\alpha/2}$ and t is time⁴. We define the normalized variability measure, $\chi =$

⁴ We note that, realistically, the power at each frequency is distributed around the above-defined powerlaw, forming an effective envelope with some

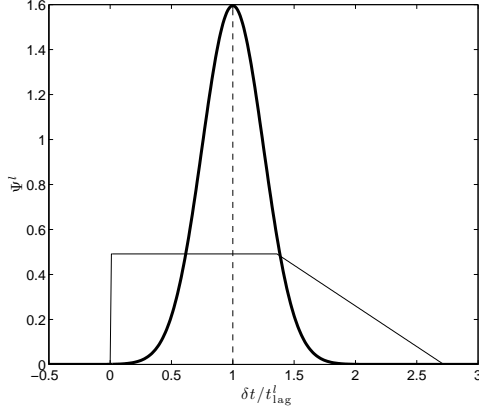


Figure 2. The emission line transfer functions used in this work to model the broad lines’ response to continuum variations (see text). While a gaussian transfer function (thick line) is relatively well localized in the time domain, the transfer function which is reminiscent of those discussed in Maoz et al. (1991) extends to much longer times. The latter transfer function naturally results in long-range correlations between line and continuum processes (whose effects are discussed in §3.2.5), and roughly characterizes the reaction of a geometrically thick BLR that is isotropically encompassing the central continuum source. We note that both transfer functions are normalized such that the line-to-continuum time-delay is $\simeq t_{\text{lag}}^l$.

$\sqrt{\sigma_f^2 - \delta^2} / \langle f \rangle$ [c.f. Kaspi et al. (2000) who express this in per-cent], where $\langle f \rangle$ is the mean flux of the light-curve, σ_f is its standard deviation, and δ is the mean measurement uncertainty of the light curve. For the Palomar-Green (PG) sample of quasars (Schmidt & Green 1983), the continuum normalized variability measure $\chi_c \sim 0.1 - 0.2$ (Kaspi et al. 2000) and, typically, $\delta \gtrsim 0.01$ (see table 1). A light-curve realization, with $\delta \ll \sigma_f$ and $\chi_c \sim 0.2$, is shown in Fig. 1.

Quasar emission occurs over a broad range of photon energies, from radio to hard X-ray wavelengths and originates from spatially distinct regions in the quasar. In the optical bands, there is some evidence for red continua to lag behind blue continua (Krolik et al. 1991; Collier et al. 1998; Sergeev et al. 2005; Bachev 2009). Without loss of generality, we associate the Y-band with the redder parts of the spectrum so that its instantaneous continuum flux may be expressed as a function of the flux in the X-band,

$$f_Y^c(t) = f_X^c * \psi^c \equiv \int_{-\infty}^{\infty} d\tau f_X^c(\tau) \psi^c(t - \tau), \quad (2)$$

where $\psi^c(\delta t)$ is the continuum transfer function⁵. Presently, ψ^c is poorly constrained by observations and only the inter-band continuum time delay, t_{lag}^c , is loosely determined (Bachev 2009, and references therein). Nevertheless, so long as $R_{\text{BLR}}/c \gg t_{\text{lag}}^c$, the particular form of ψ^c is immaterial to our discussion (see §3.2.3). For simplicity, we shall therefore take ψ^c to be a gaussian with a mean of t_{lag}^c and a standard deviation $t_{\text{lag}}^c/2$.

2.1.2. Line emission

Emission by photo-ionized (BLR) gas is naturally sensitive to the continuum level of the ionizing source. In particular,

characteristic width. We ignore this additional complication here, which introduces yet another degree of freedom in the model but does not qualitatively change the results. Real light curves are analyzed in §4.

⁵ All transfer functions, ψ , satisfy the normalization condition $\int_{-\infty}^{\infty} d(\delta t) \psi(\delta t) = 1$.

for typical BLR densities and distances from the SMBH, the response time of the photoionized gas to continuum variations is much shorter than the light travel time across the region, and so may be considered instantaneous. Therefore, the flux in some line i , which is emitted by the BLR, can be written, in the linear approximation, as

$$f_i^l = f_X^c * \psi_i^l, \quad (3)$$

where the transfer function ψ_i^l depends, essentially, on the geometry of the BLR region as seen from the direction of the observer (Horne et al. 2004, and references therein). Our present knowledge of $\psi^l(\delta t)$ for the quasar population as a whole, is, however, rather limited [see Goad et al. (1993) for a few relevant forms for ψ^l]. In what follows we shall consider two forms for the transfer function: a) a gaussian kernel with a mean t_{lag}^l and a standard deviation $t_{\text{lag}}^l/4$, and b) a transfer function with a flat core in the range $0 \leq \delta t \leq 1.36 t_{\text{lag}}^l$, with a following linear decline to zero at $\delta t = 2.72 t_{\text{lag}}^l$ (such a transfer function also results in a time-lag being $\simeq t_{\text{lag}}^l$).

The latter transfer function is motivated by the observations of the Seyfert 1 galaxy NGC 4151 (Maoz et al. 1991) and corresponds to a case where a geometrically thick, spherical shell of broad emission line gas isotropically encompasses the continuum emitting region. The different transfer functions defined above will henceforth be termed (a) the gaussian and (b) the thick-shell BLR models. The transfer functions are depicted in figure 2. The main qualitative difference between the two transfer functions, as far as light curve behavior is concerned, is that while the gaussian one is relatively localized in time, the thick shell BLR model is much broader, and results in longer range correlations between the light curves of the two bands. Unless otherwise stated, our results are presented for the gaussian model. Cases for which we find a qualitative difference between the two transfer functions are explicitly treated (e.g., §3.2.5).

A simulated light-curve of an emission line that is driven by continuum variations (assuming $t_{\text{lag}}^l = 200$ days) is shown in figure 1 (blue curves). Time-delay and smearing effects, with respect to the continuum light-curve, are clearly visible. Here too, we define a normalized variability measure for the line, χ_l , and consider $\chi_l \simeq 0.75 \chi_c$ (Kaspi et al. 2000, see their table 5). The sum of continuum and lines’ emission to the total flux in band Y is therefore given by

$$f_Y(t) = f_Y^c(t) + f_Y^l(t) = f_Y^c(t) + \sum_i f_i^l(t), \quad (4)$$

where f_Y^l is the total flux in the emission lines. While a similar expression applies, in principle, also for the total flux in band X, unless otherwise stated, we shall assume that $f_X = f_X^c$, i.e., that emission line contribution to band X is either negligible or that the line variability associated with it operates on timescales that are much too short to be resolved by the cadence of the experiment, or too long to be detectable in the time-series. For simplicity, we shall limit our discussion to a single emission line contributing to the Y-band (this restriction is relaxed in §3.2.4).

The contribution of the emission line(s) to the total flux in the Y-band requires knowledge of the equivalent width of the broad emission line, W [typically $\lesssim 100\text{\AA}$ in the optical band for strong lines (Vanden Berk et al. 2001)], the transmission curve of the broadband filter, as well as the redshift of the

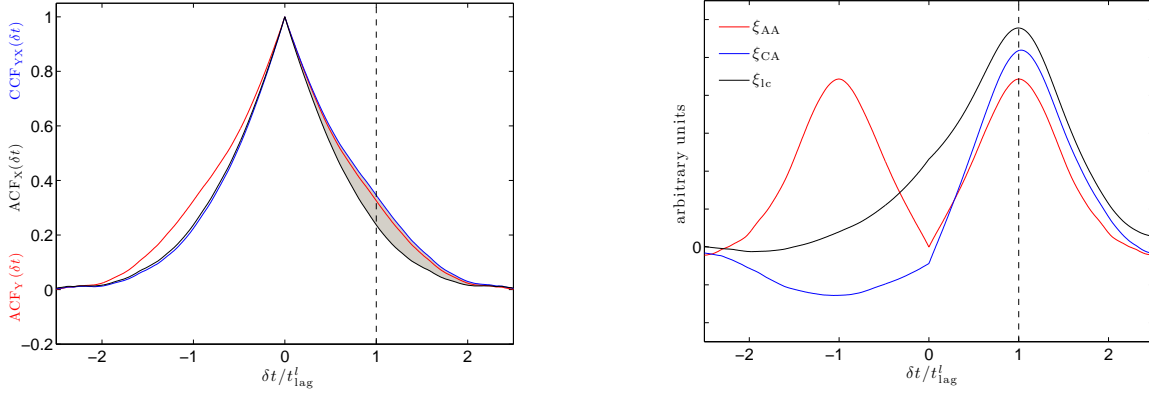


Figure 3. Statistical estimators for evaluating the line to continuum time delay. *Left:* The ACFs for the X and Y bands are shown (same color coding applies as that in Fig. 1), as well as the CCF of the two bands (black curve). Note the excess power in the ACF of the Y-band, as well as in the CCF of the two bands, relative to the ACF of the X-band (gray hatched region). This results from relatively long-range correlations between line and continuum variations, which occur on BLR light travel times. The excess power is the sought after signal (see text). *Right:* The statistical estimators, ξ_{CA} , ξ_{AA} , which quantify the excess power due to line emission, are consistent with ξ_{IC} (see legend). The position of the peaks at positive time-lags (the only ones that preserve causality) is identified with the line-to-continuum time-delay. Evidently, all methods give consistent predictions for the time-lag, which is also in agreement with the input value, t_{lag}^l (dash-dotted black line).

quasar. For example, for filters with sharp features in their response function, even small redshift changes could lead to substantial differences in the relative contribution of the emission line to the total flux in the band, η . For a flat filter response function over a wavelength range W_b (typically, $W_b \sim 10^3 \text{ \AA}$ for broadband filters), $\eta = W/W_b$. (A more accurate treatment of the line contribution to the broadband flux for the case of Johnson-Cousins filters is given in §4.) Example light-curves for the X and Y bands, assuming $\eta = 0.133$, are shown in figure 1. In the following calculations, we shall work with normalized light-curves that have a zero mean and a unit variance, i.e., $f \rightarrow (f - \langle f \rangle) / \sigma_f$.

2.2. Measuring the Line to Continuum Time Delay

The spectroscopic approach to measuring the size of the BLR cross-correlates pure line and continuum light-curves so that the position of the peak (or the center of mass) of the cross-correlation function (CCF)⁶, $\xi_{lc}(\delta t) = f_Y^c * f_Y^l$, marks the line to continuum time-delay (Peterson 1988, and references therein). However, line and continuum light curves cannot be disentangled using pure broadband photometric means and the data include only their combined signal. In fact, light-curves in different bands are rather similar due to the dominant contribution of highly correlated continuum emission processes (Fig. 1). Therefore, a naive analysis in which the CCF between the light curves of different bands is calculated would reflect more on t_{lag}^c than on t_{lag}^l (see Fig. 3).

Seeking to measure the time-delay between line and continuum processes using broadband photometric means, it is important to realize that instead of spectrally distinguishing between line and continuum light curves, it is possible, under certain circumstances, to separate these processes at the light curve level. In particular, the line light curve, $f_Y^l = f_Y - f_Y^c \simeq f_Y - f_X^c$ since $f_Y^c \simeq f_X^c$ ⁷. This is justified for quasars

since the continuum auto-correlation timescale [$\gtrsim 10^2$ days (Giveon et al. 1999), possibly reflecting on viscous timescales in the accretion flow] is much longer than t_{lag}^c [being of order days (Sergeev et al. 2005) and resulting from irradiation processes in the accretion disk, which take place on light travel time scales]. Furthermore, as $f_X = f_X^c$, $f_Y^l \simeq f_Y - f_X$, and we obtain,

$$\xi_{lc} \simeq \xi_{CA}(X, Y) \equiv (f_Y - f_X) * f_X = f_Y * f_X - f_X * f_X, \quad (5)$$

where the rightmost term is just the difference between the CCF of the light-curves and the auto-correlation function (ACF) of the light curve with the negligible line contribution (see §3.2 for cases in which emission lines contribute also to f_X). Graphically, this difference is simply the shaded region shown in the left panel of figure 3, which arises due to correlated line and continuum processes adding power on t_{lag}^l -scales. Using these statistics, and given a rather non-restrictive set of assumptions (see more in §3), it seems, in principle, possible to recover the line-to-continuum time-delay using *pure* broadband photometric data. In particular, for the example shown in figure 3, ξ_{CA} peaks at the correct time-lag, and is in agreement with the time-lag estimate as obtained using the spectroscopic method, i.e., using ξ_{lc} .

The estimator defined by equation 5 provides a good approximation for ξ_{lc} in cases where the emission line contribution to the band is sub-dominant (see below). For the more general case (e.g., when narrow band filters are concerned), it is possible to define a somewhat more generalized version where $\xi_{CA}' \equiv f_Y * f_X - (1 - \eta) f_X * f_X$, which is applicable for cases in which the emission line contribution to the Y-band is considerable or even dominant⁸. Nevertheless, with this definition, η needs to be observationally known, which is not always the case, especially when large (photometric) redshift uncertainties are concerned, the filter response function

of light curves in different bands seems to be true also for the (hidden) far-UV and optical bands given the success of the spectroscopic reverberation mapping technique in measuring line to continuum time-delays. The effects of inter-band time-delay and time-smearing of the continuum signal may account for the observed structure function differences between adjacent bands (MacLeod et al. 2010), and are further discussed in §3.2.3.

⁸ In this case, $\lim_{\eta \rightarrow 1} \xi_{CA}' = \xi_{lc}$. For $\eta \ll 1$, as appropriate for broadband photometry, $\xi_{CA}' \simeq \xi_{CA}$.

⁶ Evaluation of the cross- and auto- correlation functions is done here via the definition of Welsh (1999, see his equation 6) for the local cross-correlation function. Unless otherwise stated, we use the interpolated CCF method of Gaskell & Sparke (1986).

⁷ This is expected to be true at least for adjacent bands since the signal is largely due to continuum emission processes, such as black-body radiation, which cover a broad wavelength range. Interestingly, this broad similarity

has sharp features (Chelouche et al. 2011), or the quasar spectrum, if available, is noisy. Focusing on broadband photometric light curves in this work, the contribution of emission lines to the band is, typically, of order a few per cent (see §4). We therefore restrict the following discussion to ξ_{CA} as defined by equation 5.

It is possible to define an additional statistical estimator to measure line to continuum time-delays using broadband photometry. Specifically, by using the fact that, for broadband filters and to zeroth order approximation, $f_X \simeq f_Y$ (see Fig. 1), we may approximate ξ_{CA} by

$$\xi_{AA}(X, Y) \equiv f_Y * f_Y - f_X * f_X. \quad (6)$$

This estimator is just the difference between the ACFs of the light-curves in each band. A more intuitive way to understand the above definition may be gained by looking at figure 3, where the ACF of filter Y shows more power on t_{lag}^l timescales due to relatively long-term correlations between line and continuum processes. In contrast, the ACF of filter X , being devoid of line emission, does not show a corresponding power-excess. We note that both definitions of ξ are quasi anti-symmetric with respect to X and Y exchange.

We find that, as far as t_{lag}^l measurements are concerned, both estimators, ξ_{CA} and ξ_{AA} , give, in principle, consistent results (see Fig. 3). While ξ_{CA} has the advantage of being a more reliable estimator of ξ_{lc} (see more in §3), ξ_{AA} has the advantage of not containing a cross-correlation term of the form $f_Y * f_X$. This property allows one to evaluate ξ_{AA} even in cases where non-contemporaneous light curves are available so long as a) both light curves are adequately sampling the line transfer function, and b) quasar variability results from a stationary process (see §3.2.5). Moreover, if the variability properties for an ensemble of objects (of some given property) are statistically similar, and the auto-correlation terms, $f_Y * f_Y$ and $f_X * f_X$, are well determined in the statistical sense (see §3.1.1), then it is not required for the same objects to be observed in both bands. This opens up the possibility of monitoring different parts of the sky in each band, and using the acquired data to statistically measure the mean line to continuum time-delay. That being said, large ensembles may be required to achieve a reliable measurement of t_{lag}^l since ξ_{AA} is, in fact, an approximation to an approximation of ξ_{lc} , and its results are expected to be somewhat less reliable than both ξ_{CA} and ξ_{lc} (this is further discussed in §3).

A note is in order concerning the maximal value of $\xi_{AA}(\delta t)$ and $\xi_{CA}(\delta t)$. Unlike the spectroscopic technique where $\xi_{lc}(\delta t)$ is, in fact, the Pearson correlation coefficient and its value measures how well continuum and line processes are correlated at any δt , for the photometric estimators defined here, the peak value depends also on the relative contribution of the emission line(s) to the broad band flux. The latter depends not only on the properties of the quasar, but also on the transmission curve of the broadband filter, the variability measure of the line, and the redshift of the object. Therefore, the significance of the result is not directly implied by the value of the peak in ξ_{AA} and ξ_{CA} , and quantifying it requires a different approach, as we shall discuss in §3.4.

3. SIMULATIONS

While the reliability of the spectroscopic reverberation mapping technique has been assessed in numerous works [e.g., Gaskell & Peterson (1987) and references therein], we have yet to demonstrate it for the photometric method. In this

section we take a purely theoretical approach and use a suite of Monte Carlo simulations to test the method and quantify its strengths and weaknesses.

3.1. Sampling & Measurement Noise

All light curves are finite with respect to their duration time, t_{tot} , as well as the sampling interval, t_{sam} . This fact alone introduces potentially substantial "noise" in the cross-correlation analyses (whether photometric or spectroscopic). The effect of finite sampling is seen in Fig. 4 (left panels) where the light curves of individual objects are analyzed, showing that ξ_{CA} , ξ_{AA} formally peak at values that could be significantly removed from t_{lag}^l . This implies that even in the ideal case, where measurement noise is negligible, the deduced time-lag might be significantly offset from the true value. While similar situations occur also with spectroscopic data, our simulations indicate that the photometric estimators are, statistically, more prone to such effects.

In addition to finite sampling there is measurement noise, which reflects on the ability of any statistical estimator to recover the true time-lag with good accuracy. On an individual case basis, the effect of noise is seen to give rise to more erratic ξ_{CA} and ξ_{AA} behavior, potentially leading to substantial deviations in the position of the peak from the true time-lag. In fact, for the particular case shown (Fig. 4), ξ_{CA} has a kink at t_{lag}^l and peaks only at $\sim 3t_{lag}^l$. In this particular case, ξ_{AA} happens to be less affected by noise, and formally peaks at $\sim 1.15t_{lag}^l$ due to a narrow feature being the result of noise.

Sampling and measurement noise are manifested as small scale fluctuations in all statistical estimators. In particular, in some cases (see Figs. 4 & 5), large amplitude fluctuations are observed, which peak at long timescales, $\delta t / t_{lag}^l > 1$, and their value could exceed the value of the true peak (i.e., that which is associated with, and peaks at, $\sim t_{lag}^l$). Clearly, an algorithm that would aid to properly identify the relevant signal, would be of advantage. To this end we use a physically-motivated algorithm related to the geometry of the BLR: the fact that the BLR encompasses the continuum emitting region means that the width of its line transfer function should be of order the time-lag. Therefore, one expects the relevant signal in ξ_{CA} , ξ_{AA} to peak at t_{lag}^l with a width, $\Delta(\delta t) \sim t_{lag}^l$. In particular, narrower features with $\Delta(\delta t) / t_{lag}^l \ll 1$ are likely to be merely the result of noise or sampling, and although they could reach large amplitudes, they are of little relevance to the time-lag measurement.

The aforementioned properties of the line transfer function motivate us to consider the following algorithm to aid in the identification of the time-lag: we resample ξ_{CA} and ξ_{AA} onto a uniform logarithmic grid, which preserves resolution in $\Delta(\delta t) / \delta t$ units. We then apply a running mean algorithm such that the boxcar size corresponds to a fixed range in logarithmic scale. This procedure smooths out narrow features having $\Delta(\delta t) / \delta t \ll 1$. Examples for smoothed statistical estimators are shown for two levels of noise in figure 5. Clearly, narrow features at large δt are significantly suppressed without diminishing the power of similar $\Delta(\delta t)$ features centered at smaller δt . It should be noted, however, that using this technique does not assure that the correct time-lag is recovered (see above). Furthermore, in some cases, multiple peaks may be found and additional methods are required to assess their significance (see §4).

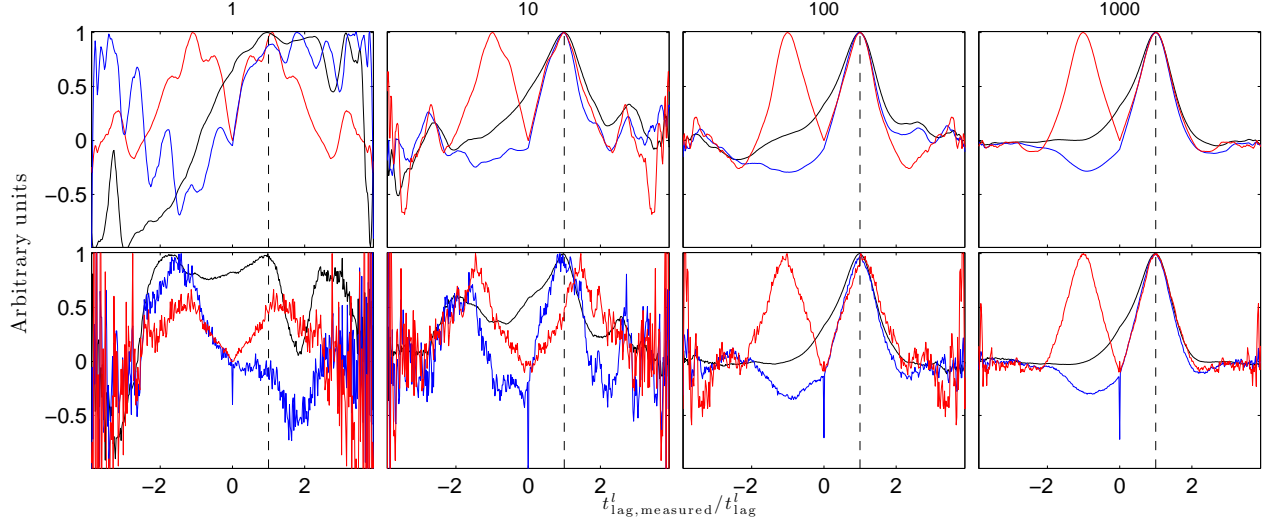


Figure 4. Averages of ξ_{CA} (blue), ξ_{AA} (red) as well as for ξ_{ic} (black) for ensembles of statistically equivalent quasars (the number of objects in each ensemble is indicated above each column). Upper (lower) panels correspond to a noise-level $\delta/\langle f \rangle = 0$ (0.03). In all simulations the total duration of the light curve is $4t_{lag}^l$, and visits are $t_{lag}^l/50$ apart. The relative contribution of the emission line to the filter flux, $\eta \simeq 0.13$. Clearly, finite sampling of the light curves, even in the absence of measurement noise, could result in the peaks being offset with respect to t_{lag}^l . This is true for individual objects as well as for small samples. Generally, however, upon averaging over many objects, the mean estimators peak at $\delta t \simeq t_{lag}^l$ (right panels). When measurement noise is present, larger ensemble are required for the peak of the $\langle \xi_{CA} \rangle$, $\langle \xi_{AA} \rangle$ and $\langle \xi_{ic} \rangle$ to coincide with t_{lag}^l to good accuracy (e.g., compare the top and bottom panels in the second column from the left). Overall, the photometric and the spectroscopic estimators give consistent results, which is especially true for large ensembles.

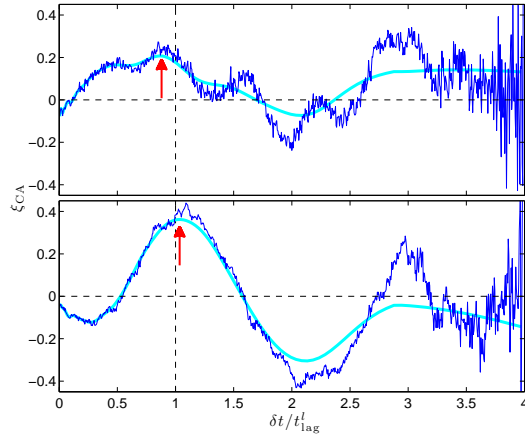


Figure 5. Photometric time-lag measurements for individual quasars having noisy data ($\delta/\langle f \rangle = 0.03/0.01$ in the top/bottom panel). Calculated ξ_{CA} 's (blue curves) show multiple peaks, some of which are narrow and peak at $\delta t > t_{lag}^l$, potentially with large amplitudes (note the feature at $\delta t/t_{lag}^l \simeq 3$). Smoothing of the signal using a running mean algorithm over a uniform logarithmic grid suppresses narrow features and highlights the peak associated with the time lag (cyan curves; see text). Red arrows mark the peak at $t_{lag,measured}^l$, which, in this example, deviates only slightly from the input lag (dashed vertical line at $\delta/t_{lag}^l = 1$).

Testing for the accuracy of time-lag measurements using noisy data, we have conducted uniformly sampled light curve simulations of a quasar (100 realizations were used having 800 points in each light curve, with a total light curve duration, t_{tot} , satisfying $t_{tot}/t_{lag}^l = 5$ and $\eta \sim 0.13$) at several levels of measurement noise. For each realization, ξ_{CA} was calculated and δt where it peaks was identified with $t_{lag,measured}^l$ and logged. The resulting time-lag statistics are shown in figure 6. The distribution is clearly non-gaussian and shows a peak at the input time lag with a tail extending to long time-lags. Not unexpectedly, the dispersion in time-lag measurements

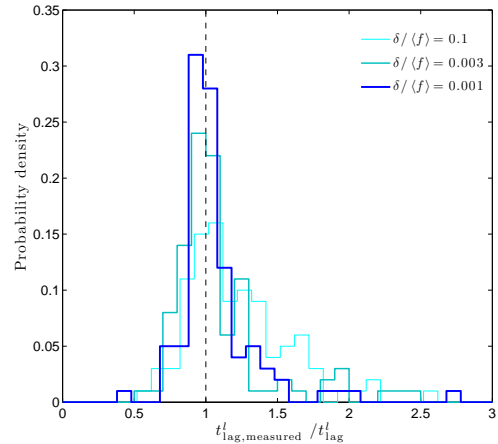


Figure 6. Measured time-lag distributions for a sample of 100 quasars (having 800 points in each light curve and with $t_{tot}/t_{lag}^l = 5$; $\eta \simeq 0.13$ was assumed), and for several noise levels (see legend). Clearly, for all cases, the distributions peak at the input time lag (dashed line), demonstrating the feasibility of the photometric approach for time-lag measurement. As expected, noisier light curves result in broader time lag distributions. The distributions show a tail extending to large $t_{lag,measured}^l/t_{lag}^l$ -values and are clearly non-gaussian.

increases with the noise level. For the particular examples shown, taking $\delta/\langle f \rangle = 0.01$ [a noise level typical of photometric light curves of quasars (Kaspi et al. 2000)], $\sim 60\%$ of the measurements will result in $t_{lag,measured}^l$ being within $\pm 10\%$ of the true lag. For noisier data with $\delta/\langle f \rangle = 0.1$, only $\sim 30\%$ of all realizations result in a time lag within $\pm 10\%$ of the true time lag. These calculations demonstrate that photometric reverberation mapping in the presence of measurement noise typical of photometrically monitored quasars is indeed feasible, and that the measurement is, in principle, reliable. When noisier data are concerned, the uncertainty on the time-lag is larger.

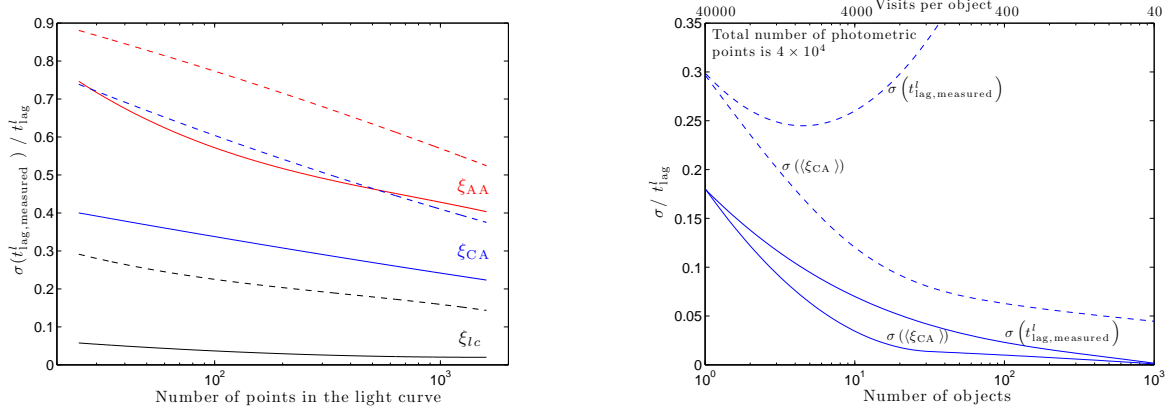


Figure 7. Relative measurement uncertainties on t_{lag}^l . *Left:* One standard deviation of the measured time-lag distribution functions (i.e., the uncertainty on $t_{\text{lag,measured}}^l$) as obtained by measuring the time delay for individual realizations in a large ensemble of objects (having the same BLR size and sampling characteristics as those of figure 5). One hundred simulations were used to calculate each data point (6 equally log-spaced points were calculated in each curve and a second degree polynomial fit to the results is shown). Noise level $\delta/\langle f \rangle = 0.01$ (0.1) is shown in solid (dashed) lines, and the usual color coding scheme applies ($\xi_{CA}/\xi_{AA}/\xi_{lc}$ results in blue/red/black curves). Clearly, better signal-to-noise is obtained by either reducing the measurement noise or by better sampling the light curve. Generally, ξ_{CA} is the more reliable photometric estimator, while both photometric methods are less accurate than the spectroscopic one (ξ_{lc}). *Right:* The uncertainty on the mean time-lag deduced for an ensemble of objects using ξ_{CA} , for two noise levels ($\delta/\langle f \rangle = 0.01, 0.1$ are shown in solid and dashed curves, respectively, and smoothing was applied). The total observing effort (number of points for the entire sample) was held fixed. The time-lag was deduced in two ways: (1) by measuring the time-lag for individual objects with the ξ_{CA} estimator and taking the mean result (thin lines), and by measuring the position of the peak of $\langle \xi_{CA} \rangle$ (thick lines). The uncertainty on the mean time-lag reported for the latter quantity was deduced from multiple simulations of statistically equivalent ensembles. The results show that, for the same observing effort, monitoring more objects with lower cadence (so long as the line transfer function is properly sampled) results in more accurate time-lag measurements. Also, measuring the peak in the mean statistical estimator provides more accurate results than measuring the time-lag for individual objects [$\sigma(\langle \xi_{CA} \rangle) < \sigma(t_{\text{lag,measured}}^l)$].

To better quantify the ability of the photometric method to uncover the time-lag under various observing strategies, we repeated the above analysis for two noise levels ($\delta/\langle f \rangle = 0.01, 0.1$) while varying the number of points in the light curves (i.e., observing visits). More specifically, we maintained a fixed $t_{\text{tot}}/t_{\text{lag}}^l = 5$ and varied the sampling period, t_{sam} (we made sure that $t_{\text{lag}}^l/t_{\text{sam}} \geq 5$ so that the BLR transfer function is never under-sampled). Monte Carlo simulations were carried out to obtain reliable statistics, and we report the one standard deviations of the measured time-lag distributions, $\sigma(t_{\text{lag,measured}}^l)$, in figure 7 (also shown, for comparison, are the corresponding ξ_{lc} -statistics). As expected, better sampled light curves result in a lower dispersion in $t_{\text{lag,measured}}^l$ for all statistical methods. Also, unsurprisingly, ξ_{CA} is the more reliable photometric estimator for the time-lag, and both photometric estimators are worse than ξ_{lc} . In particular, quasar light curves having ~ 100 points in each filter with photometric errors of order 1% result in a ξ_{CA} -deduced time-lag dispersion of order $\sim 35\%$. Similar quality light curves can be found in the literature (Giveon et al. 1999; Kaspi et al. 2000), and are analyzed in §4.

Consider the following question: having finite resources, is it better to observe fewer objects with better cadence or more objects having sparser light curves? [We assume that the cadence is adequate for sampling the line transfer function (see more in §3.2), and that the same signal-to-noise is reached in both cases.] The answer to this question is given in figure 7 (right panel) where the total number of visits was kept fixed yet the number of objects in the ensemble varied (correspondingly, the number of visits per object changed to maintain their product constant). Interestingly, for the same observing effort, it is advantageous to observe more objects with worse cadence. Using this strategy, one is less sensitive to unfavorable variability patterns of particular quasars. For the case considered here, the time-lag uncertainty drops

by a factor ~ 3 by increasing the sample size from one to ten objects (the uncertainty for the case of ensembles was determined from Monte Carlo simulations of many statistically similar ensembles). Similar results are obtained also for ξ_{AA} (not shown).

3.1.1. Ensemble averages

In the upcoming era of large surveys, statistical information may be gathered for many objects. For example, the LSST is expected to provide photometric light curves for $> 10^6$ quasars having a broad range of luminosities and redshifts. With such large sets of data at one's disposal, sub-samples of quasars may be considered having a prescribed set of properties (e.g., luminosity and redshift), and the line to continuum time-lag measurement may be quantified for the ensembles. In this case, it is possible to measure the characteristic line-to-continuum time-delay in two ways: by measuring the peak of $\xi_{CA}(\delta t)$ or $\xi_{AA}(\delta t)$ on a case by case basis and then constructing time-lag distributions to measure their moments, or by defining the ensemble averages of the statistical estimators. Specifically, we define $\langle \xi_{CA}(\delta t) \rangle$, $\langle \xi_{AA}(\delta t) \rangle$ as the arithmetic averages⁹ of the corresponding statistical estimators at every δt . (Alternative definitions for the mean do not seem to be particularly advantageous and are not considered here.) The average statistical estimators for ensembles of varying sizes are shown in figure 4. As expected, averaging leads to a more robust measurement of the peak, as the various $\xi_{CA}(\delta t)$'s "constructively-interfere" at $\sim t_{\text{lag}}^l$. The ensemble size required to reach a time-lag measurement of a given accuracy naturally depends on the noise level.

We find that measuring the time-lag from the peak of $\langle \xi_{CA} \rangle$ (or $\langle \xi_{AA} \rangle$) is more accurate than measuring the time-lags for

⁹ We similarly define, for comparison purposes, $\langle \xi_{lc}(\delta t) \rangle$. These definitions were, in fact, previously used to compute the curves shown in figure 3.

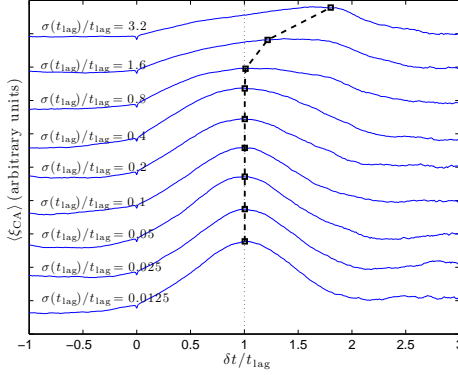


Figure 8. The effect of scatter in the broad line region properties on (arbitrarily scaled) $\langle \xi_{CA}(\delta t) \rangle$. A large ensemble of objects (typically 100-1000) was used, whose time-lag distribution follows a modified Gaussian (see text), which is characterized by the mean time-lag, t_{lag} and its standard deviation, $\sigma(t_{lag})$. $t_{tot}/t_{lag} = 4$ was assumed. For $\sigma(t_{lag})/t_{lag} < 1$, the distribution is nearly Gaussian, $\langle \xi_{CA}(\delta t) \rangle$ is, likewise, symmetric, and its peak is at t_{lag} . For $\sigma(t_{lag})/t_{lag} \geq 1$, the time-lag distribution is, by definition, modified (see text), and the effective mean time lag is $> t_{lag}$ (black squares for each curve). This, and the fact that, for some objects, $t_{lag} \sim t_{tot}$ (hence the line transfer function is poorly sampled) result in an asymmetric $\langle \xi_{CA}(\delta t) \rangle$, which only roughly peaks at the effective mean time lag.

individual objects in the ensemble, and then quantifying the moments of the distribution (Fig. 7)¹⁰. This is particularly important when noisy data are concerned, in which case reliable time-lag measurements for individual objects are difficult if not impossible to obtain. To see this, we note the rising uncertainty on the deduced time-lag, $\sigma(t_{lag,measured}^l)$, as the number of visits per object is reduced (and despite the fact that a correspondingly larger sample of objects is considered; see the right panel of Fig. 7 for a case in which $\delta/\langle f \rangle = 0.1$). In contrast, when working with $\langle \xi_{CA} \rangle$ -statistics, the uncertainty monotonically declines so long as the sampling of the transfer function is adequate.

The above analysis highlights the importance of using large samples of objects (even with less than ideal sampling) in addition to studying individual objects having relatively well-sampled light curve. In particular, by using large enough samples of quasars, the effects of noise, and even sparse sampling, may be overcome.

Current studies suggest that there is a scatter of 30%-40% in the BLR size vs. quasar luminosity relation (Bentz et al. 2009; Kaspi et al. 2000). To assess the effect of such a scatter on $\langle \xi_{CA} \rangle$ (similar results apply also for $\langle \xi_{AA} \rangle$), we averaged the results for an ensemble of simulated objects whose time-lags follow a Gaussian distribution with a mean t_{lag} and standard deviation $\sigma(t_{lag})$. We modify this Gaussian such that the input lag is always positive definite: for $\sigma(t_{lag})/t_{lag} \ll 1$ the distribution is Gaussian while for $\sigma(t_{lag})/t_{lag} \sim 1$ there is an excess of systems with zero lag. $\langle \xi_{CA}(\delta t) \rangle$, is shown in figure 8: evidently, the average statistical estimator peaks at the mean of the distribution so long as $\sigma(t_{lag})/t_{lag} < 0.8$. For larger ratios, the distribution considerably deviates from Gaussian and its mean is $> t_{lag}$. In this case, $\langle \xi_{CA}(\delta t) \rangle$ still peaks around the mean but its shape is highly asymmetric.

¹⁰ The uncertainty on the time-lag, as deduced from $\langle \xi_{CA} \rangle$, was calculated by simulating numerous statistically-equivalent ensembles of objects, calculating $\langle \xi_{CA} \rangle$, and measuring the time-lag from its peak. A time-lag distribution is obtained with the uncertainty given by its standard deviation, $\sigma(\langle \xi_{CA} \rangle)$.

This is partly due to the time-lag distribution, but also so due to the fact that the transfer functions with the largest t_{lag}^l 's are not adequately sampled by the light curve ($t_{tot}/t_{lag}^l = 4$ was assumed). To conclude, photometric reverberation should yield accurate mean BLR sizes for a sample of quasars, given the observed scatter in the BLR properties.

3.2. Systematics

We identified several potentially important biases in the method, which we shall now quantify using a suite of Monte Carlo simulations. We work in the limit of large ensembles so that the effect of sampling and measurement noise are negligible (typically, the results of several hundreds of realizations are averaged over and the line to continuum time delay is identified with the peak of $\langle \xi_{CA}(\delta t) \rangle$ and $\langle \xi_{AA}(\delta t) \rangle$).

3.2.1. Measurement noise

Biases are present in the time-lag measurement from noisy data. These are negligible for noise levels $\delta/\langle f \rangle < \eta$ but may surface otherwise. Specifically, for a (Gaussian) noise level of $\sim 50\%$, and a relative line contribution to the band of 10%, both photometric estimators over-estimate t_{lag}^l by as much as 20% with ξ_{AA} being more biased than ξ_{CA} (Fig. 9). This bias could therefore be present in situations where large and noisy ensembles are considered, or when weak emission lines are targeted. Quantifying the bias requires good understanding of the noise properties.

A related bias exists when the noise level in the two bands differs substantially. More specifically, when $|\delta_X/\langle f_X \rangle - \delta_Y/\langle f_Y \rangle| \sim \eta$ (δ_X/δ_Y is the noise level in the X-/Y- bands), our simulations show that $t_{lag,measured}$ may differ from t_{lag} by as much as 25%. Whether an over-estimate or an under-estimate of t_{lag} is obtained depends on the particular noise properties, as mentioned above. Observationally, one should therefore aim to work with data having comparable noise levels for the different bands to obtain a bias-free result. As noted above, for relatively strong lines or low noise levels, such biases are negligible.

Varying seeing conditions leading to aperture losses, as well as improperly accounting for stellar variability in the field of the quasar, could lead to correlated errors between the bands. This in turn could lead to artificial zero-lag peaks in the correlation function of the light curves (Welsh 1999), and several solutions have been devised to overcome this problem (Alexander 1997; Zu et al. 2011, and references therein). Nevertheless, the formalism developed here subtracts off, by construction, the contribution of similar processes (e.g., correlated noise) to both light curves. In fact, as far as the algorithm is concerned, the continuum contribution to the Y-band is merely an effective correlated noise to be corrected for, which it does. Therefore, photometric reverberation mapping, as proposed here, is considerably less susceptible to the effects of correlated noise than the spectroscopic method. That being said, if the noise between the bands correlates over sufficiently long (e.g., \gg day) timescales, a secure detection of the line-to-continuum time delay may be more challenging (for an effectively similar case see §3.2.3).

3.2.2. Sampling

Sampling is rarely uniform. In fact, seasonal gaps could be of the order of the time lag in some objects (Kaspi et al. 2000). The full treatment of sampling related issues is beyond the scope of this paper, and we restrict our discussion to

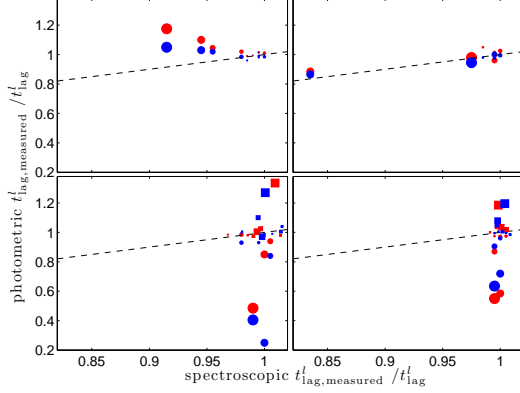


Figure 9. Biases in measuring line to continuum time delays as calculated for the spectroscopic (abscissa) and photometric methods (ordinate). Dashed line is for a 1:1 ratio. Upper-left panel shows the effect of noise with the largest data point [blue (red) reflecting on ξ_{CA} -(ξ_{AA} -) deduced measurements] corresponding to $\delta/\langle f \rangle = 0.512$ with subsequently smaller size symbols corresponding to values smaller by a factor 2 (the same symbol-size value applies to all panels). Upper-right panel shows the bias as a function of t_{gap} and implies consistency between the spectroscopic and photometric results (largest symbol is for $t_{\text{gap}}/t_{\text{lag}}^l = 2$). Lower-left panel quantifies the bias for the X-band leading (circles) or trailing (squares) the Y-band. Largest symbol is for $|t_{\text{lag}}^c|/t_{\text{lag}}^l \simeq 0.3$. Lower-right panel shows the bias in the presence of a subordinate emission line whose time-lag is $t_{\text{lag}}^l/2$, which is contributing to the Y (circles) and to the X (squares) filter. The largest symbol corresponds to $\eta_s/\eta = 0.8$ (see text).

light curve gaps (real data are treated in §4). To check for potential systematics, we resampled our simulated light curves with equal “on” and “off” observing periods with durations t_{gap} . We identify a bias when $t_{\text{gap}} \simeq t_{\text{lag}}^l$. Nevertheless, both the spectroscopic and the photometric methods are equally affected by it so that their results remain consistent. As our aim is to focus on cases in which the photometric approach leads to new or different biases, we do not further quantify this bias¹¹.

3.2.3. Inter-band continuum time delays

Thus far, $t_{\text{lag}}^c \ll t_{\text{lag}}^l$ was assumed. While the spectroscopic method is unaffected by inter-band continuum delays (the continuum in the immediate vicinity of the emission line is considered), our definition of the continuum is that which corresponds to the filter having the least contribution of emission lines to its flux, i.e., the X-band.

For a large set of simulation runs (obtained by varying both η and $t_{\text{lag}}^c/t_{\text{lag}}^l$; not shown), we find that biases become non-negligible for $\eta^{-1}|t_{\text{lag}}^c|/t_{\text{lag}}^l \gtrsim 1$ ($t_{\text{lag}}^c > 0$ implies that continuum emission in the Y-band lags behind the X-band). Here we consider particular cases in which $|t_{\text{lag}}^c|/t_{\text{lag}}^l \leq 0.3$ ($\eta \simeq 0.13$ is assumed), and find that $|t_{\text{lag}}^c|/t_{\text{lag}}^l \gtrsim 0.1$ results in substantial, $> 20\%$ bias (Fig. 9) for the following reason: although modest values of $|t_{\text{lag}}^c|/t_{\text{lag}}^l$ are considered, the contribution of continuum processes to both light curves by far exceeds that of the emission line. Specifically, when the continuum in the Y-band lags behind the X-band, the deduced time lag reflects more on t_{lag}^c than on t_{lag}^l . When the X-band lags behind the Y-band, and $t_{\text{lag}}^c/t_{\text{lag}}^l$ is significant, the peak in both statisti-

cal estimators is strongly suppressed and time-lag measurements become less reliable. Realistically, inter-band continuum time-delays seem to be of order $10^{-2}t_{\text{lag}}^l$ (Bachev 2009), and it is therefore likely that biases of the type discussed here would be negligible for most strong broad emission lines.

3.2.4. Multiple emission lines

Realistic quasar spectra could result in more than one emission line contributing to the Y-band, or even different emission lines contributing to both bands. While such complications are irrelevant for the spectroscopic method (note the small statistical scatter around unity in Fig. 9), the photometric method is only sensitive to the combined contribution of all emission processes in some waveband. Here we study the biases introduced by including the contribution of a weaker secondary emission line to either of the bands whose time lag, $t_{\text{lag},s}^l \neq t_{\text{lag}}^l$.

We find potentially considerable biases when the relative contribution of the weaker line to the flux, η_s satisfies $\eta_s/\eta \lesssim 1$. However, the magnitude of the bias is also affected by $(t_{\text{lag},s}^l - t_{\text{lag}}^l)/t_{\text{lag}}^l$. We do not attempt to fully cover the parameter space in this work, and focus on particular cases. Figure 9 shows an example with $t_{\text{lag},s}^l/t_{\text{lag}}^l = 0.5$ where we find $\gtrsim 20\%$ biases for $\eta_s/\eta \gtrsim 0.5$: when the weaker line contributes to the Y-band, $t_{\text{lag},\text{measured}}^l < t_{\text{lag}}^l$ while the opposite occurs when the weaker line contributes to the X-band. Comparing to a case in which $t_{\text{lag},s}^l = t_{\text{lag}}^l/10$ and $\eta_s/\eta = 0.8$, we find similar trends but an overall smaller ($< 5\%$) bias. Assuming instead $t_{\text{lag},s}^l = 2t_{\text{lag}}^l$ and $\eta_s/\eta = 0.8$, we find a bias of order 20% (10%) when the weaker line contributes to the Y- (X-) band. While the magnitude of the bias is clearly not solely determined by η/η_s , we find that the bias is, generally, small for $\eta_s/\eta \ll 1$. Clearly, if $t_{\text{lag},s}^l \ll t_{\text{sam}}$ or $t_{\text{lag},s}^l \gg t_{\text{tot}}$ then the time-series is insensitive to the presence of the secondary line, and the bias would be negligible regardless of η_s/η .

Further quantifying the bias as a function of the line properties (e.g., transfer functions and time-delays), filter response functions, quasar redshifts, and observing patterns is beyond the scope of this paper, and should be carried out on a case by case basis.

3.2.5. Total light curve duration

It is well known that the ratio of the total duration of the light curve to the time-lag, $t_{\text{tot}}/t_{\text{lag}}^l$, needs to be greater than some value to be able to adequately sample the transfer function and reliably measure the time lag using spectroscopic means. Our calculations demonstrate that the same holds also for the photometric method. In particular, for the gaussian (thick shell) transfer function, reliable measurements require that $t_{\text{tot}}/t_{\text{lag}}^l \gtrsim 3$ (9); see figure 10.

Differences between the photometric and the spectroscopic approach arise for $t_{\text{tot}}/t_{\text{lag}}^l \gg 1$: while the spectroscopic method gradually converges to t_{lag}^l (assuming sufficient data and adequate sampling; see Fig. 10), the photometrically deduced time lag, $t_{\text{lag},\text{measured}}^l$, develops a bias with respect to t_{lag}^l with increasing $t_{\text{tot}}/t_{\text{lag}}^l$. Generally, the bias is comparable (but not identical) for $\langle \xi_{CA} \rangle$ and $\langle \xi_{AA} \rangle$, and over-estimate the true lag. We quantify the bias for the two line transfer functions, ψ^l , defined above (§2.1.2), and find it to be different

¹¹ See §4 for the usage of discrete correlation functions, which are less susceptible to sampling issues.

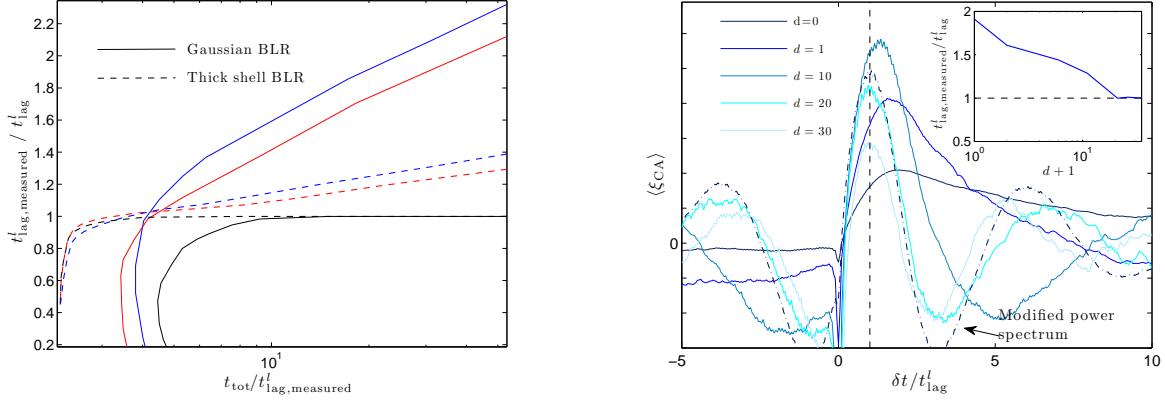


Figure 10. *Left:* the bias in the time-lag measurement as a function of the observable quantity $t_{\text{tot}}/t_{\text{lag,measured}}^l$ ($\xi_{\text{CA}}/\xi_{\text{AA}}/\xi_{\text{LC}}$ results are shown in blue/red/black curves). For all statistical estimators there is a minimum $t_{\text{tot}}/t_{\text{lag,measured}}^l$ below which the sampling is inadequate. Above this threshold, the spectroscopic method converges to the input time lag (e.g., for a gaussian transfer function, $t_{\text{lag,measured}}^l \simeq t_{\text{lag}}^l$ for $t_{\text{tot}}/t_{\text{lag,measured}}^l > 3$). In contrast, there is a bias using either photometric method wherein $t_{\text{lag,measured}}^l/t_{\text{lag}}^l$ is a rising function of $t_{\text{tot}}/t_{\text{lag,measured}}^l$, and is more pronounced for geometrically thick BLR configurations. *Right:* a particular example for $\langle \xi_{\text{CA}}(\delta t) \rangle$, calculated for an ensemble of 100 statistically identical objects with $t_{\text{tot}}/t_{\text{lag}}^l = 50$, resulting in a peak at $\delta t \simeq 2t_{\text{lag}}^l$ (dark-black solid line). When the light curves of both bands are de-trended by a polynomial of degree d , the bias is gradually removed. For large enough d -values, substantial power on relevant timescales is removed, thereby affecting the significance of the results (see legend). When the quasar power-spectrum is truncated at frequencies $\omega < \omega_{\text{min}}$ [here $(2\pi/\omega_{\text{min}})/t_{\text{tot}} \simeq 0.13$], the light curve appears to be stationary, and the bias disappears (dash-dotted dark blue line).

in each case: broader ψ^l that extend over larger δt intervals, lead to more biased results. For example, while the thick shell BLR model shows a factor ~ 2 bias for $t_{\text{tot}}/t_{\text{lag,measured}}^l = 50$, the corresponding bias for the Gaussian BLR is only $\sim 40\%$ (see Fig. 10). The bias is seen to grow logarithmically with $t_{\text{tot}}/t_{\text{lag,measured}}^l$, and so would be most prominent when analyzing long time-series of low-luminosity quasars. Considering, for example, ~ 10 years of LSST data for a low- z quasar with a thick shell BLR whose size is ~ 100 light-days. In this case, $t_{\text{tot}}/t_{\text{lag}}^l \sim 30$, which would result in $t_{\text{lag,measured}}^l/t_{\text{lag}}^l \sim 2$. Not correcting for this bias would lead to an over-estimation of the black hole mass, by a similar factor, with considerable implications for black hole formation and evolution.

Consider the bias in $\langle \xi_{\text{CA}} \rangle$: as its value is sensitive to the line transfer function, its origin may be traced to the $f_Y * f_X$ term in Eq. 5, which is akin to the bias discussed in Welsh (1999). In a nutshell, with the quasar's power spectrum being red, most of the power is associated with the lowest frequency modes. Nevertheless, those are the same modes that are not adequately sampled by any finite time series. As such, the data *appear* to originate in a non-stationary process where, for example, the mean flux changes substantially between the extreme ends of the light curve. This and the fact that emission lines' contribution to the flux is always additive results in a positive bias. More extended line transfer functions, resulting in longer term correlations between the light curves, are therefore more prone to such biases. With $\langle \xi_{\text{AA}}(\delta t) \rangle \simeq \langle \xi_{\text{CA}}(\delta t) \rangle$, similar biases are also encountered there, that trace back to the $f_Y * f_Y$ term.

To verify the source of the bias, we repeated the calculations using a truncated form for the power-spectrum where all frequencies below a minimum frequency, ω_{min} , have no power associated with them (we have experimented with $2\pi/t_{\text{lag}} \gg \omega_{\text{min}} \gg 2\pi/t_{\text{tot}}$). The resulting $\langle \xi_{\text{CA}}(\delta t) \rangle$ is indeed unbiased and peaks at t_{lag}^l (not shown). For intermediate cases where, for example, the power spectrum flattens at low frequencies (Czerny et al. 1999), the results will be less biased but may not be entirely bias-free.

Having identified the source of the bias, it is now possible to correct for it using one of several methods which we term: de-trending, sub-sampling, and bootstrapping. De-trending has been shown to be useful to correct for biases in the spectroscopic method (Welsh 1999). Basically, one filters out long-term trends in the light curve by fitting (done here in the least-squares' sense) and subtracting off a polynomial of some degree, d , from the data. As a polynomial of degree d has d zeros, subtracting a higher degree polynomial from the data results in a suppressed variance at frequencies $\omega \lesssim d(2\pi/t_{\text{tot}})$. Conversely, the highest degree polynomial that can be subtracted from the data, whilst not suppressing the reverberation signal, is $d \lesssim [t_{\text{tot}}/t_{\text{lag}}]$. The effect of de-trending is shown in figure 10 for a range of d -values, and assuming $t_{\text{tot}}/t_{\text{lag}}^l = 50$. While subtracting a $d = 2$ polynomial already decreases the bias substantially, a bias-free result is recovered by de-trending with a $d = 20$ ($= 0.4t_{\text{tot}}/t_{\text{lag}}^l$) polynomial. Further increasing d suppresses the sought after signal to insignificant levels by removing modes with frequencies $\sim 2\pi/t_{\text{lag}}^l$. The dependence of the remaining bias on the de-trending polynomial degree, d , is shown in the inset of figure 10.

An alternative method to remove the bias is to analyze continuous sub-samples of the time series, thereby reducing the effective t_{tot} and decreasing the bias. This method can be implemented in cases where one is not data-limited.

The third method for removing the bias involves bootstrapping: given an observed continuum light curve (i.e., f_X), and an assumed ψ^l , the light curve of the line-rich band is simulated. Upon sampling it using the cadence of the real data, an artificial f_Y light curve is obtained. By calculating the statistical estimators for the semi-artificial data, it is possible to compare $t_{\text{lag,measured}}^l$ to the input lag, and correct for the bias. Conversely, should the bias be known by other means, inferences concerning the nature of the line transfer function may be obtained.

Table 1
Photometric properties of the PG sample of quasars^(a)

Object Name (1)	z (2)	$\lambda L_{\lambda}(5100\text{\AA})$ ($10^{44} \text{ erg s}^{-1}$) (3)	B pts (4)	χ_B (5)	$\langle \delta_B \rangle$ (6)	R pts (7)	χ_R (8)	$\langle \delta_R \rangle$ (9)	net w/Fe (10)	net w/Fe (11)	H α lag ^(b) (days) (12)	Predicted lag (days) (13)	Photo. lag (days) (14)
PG 0026+129	0.142	7.0 ± 1.0	70	0.19	0.02	71	0.14	0.02	0.03	0.07	132^{+29}_{-31}	147 ± 25	-
PG 0052+251	0.155	6.5 ± 1.1	75	0.26	0.03	75	0.20	0.02	0.04	0.08	211^{+66}_{-44}	141 ± 27	-
PG 0804+761	0.100	6.6 ± 1.2	83	0.17	0.01	88	0.14	0.01	0.05	0.07	193^{+16}_{-17}	136 ± 27	200 ± 100
PG 0844+349	0.064	1.72 ± 0.17	65	0.10	0.02	66	0.10	0.02	0.08	0.06	39^{+16}_{-16}	51 ± 6	500 ± 200
PG 0953+414	0.239	11.9 ± 1.6	60	0.14	0.03	60	0.12	0.01	0.06	0.11	187^{+27}_{-33} (c)	231 ± 39	-
PG 1211+143	0.085	4.93 ± 0.80	25	0.16	0.01	24	0.13	0.01	0.06	0.07	116^{+38}_{-46}	109 ± 20	-
PG 1226+414	0.158	64.4 ± 7.7	45	0.12	0.01	45	0.10	0.01	0.04	0.08	514^{+65}_{-64}	703 ± 135	-
PG 1229+204	0.064	0.94 ± 0.10	44	0.16	0.03	45	0.16	0.03	0.08	0.06	71^{+39}_{-46}	34 ± 4	N/A
PG 1307+085	0.155	5.27 ± 0.52	30	0.14	0.01	30	0.10	0.01	0.04	0.08	179^{+94}_{-145}	122 ± 16	-
PG 1351+640	0.087	4.38 ± 0.43	35	0.11	0.01	35	0.10	0.01	0.06	0.07	247^{+162}_{-78}	101 ± 13	-
PG 1411+442	0.089	3.25 ± 0.28	29	0.10	0.01	29	0.07	0.01	0.06	0.07	103^{+40}_{-37}	82 ± 9	-
PG 1426+015	0.086	4.09 ± 0.63	26	0.16	0.01	25	0.13	0.02	0.06	0.07	90^{+46}_{-52}	96 ± 17	-
PG 1613+658	0.129	6.96 ± 0.87	66	0.11	0.01	64	0.10	0.02	0.04	0.07	43^{+40}_{-22}	144 ± 22	300 ± 130
PG 1617+175	0.114	2.37 ± 0.41	56	0.19	0.02	56	0.14	0.02	0.04	0.07	111^{+31}_{-37}	67 ± 12	-
PG 1700+518	0.292	27.1 ± 1.9	53	0.07	0.02	53	0.07	0.01	0.05	0.11	114^{+246}_{-235} (c)	428 ± 61	300 ± 160
PG 1704+608	0.371	35.6 ± 5.2	38	0.13	0.01	40	0.11	0.01	0.02	0.05	437^{+252}_{-391} (c)	550 ± 109	400 ± 200
PG 2130+099	0.061	2.16 ± 0.2	78	0.10	0.02	79	0.08	0.02	0.08	0.06	237^{+53}_{-28}	60 ± 7	240 ± 100

Columns: (1) Object name, (2) redshift, (3) monochromatic luminosity in units of $10^{44} \text{ erg s}^{-1}$, (4)-(6) properties of the photometric light curve of the B -band: number of points, the normalized variability measure, and the mean measurement uncertainty. (7)-(9) having the same meaning as (4)-(6) but for the R band. (10) the net contribution of emission lines to the bands excluding the iron blends. (11) like (10) but including the iron emission complexes. (12) the spectroscopically measured time lag for the H α line from Kaspi et al. (2000). (13) The *observed* lag for the Balmer emission lines as predicted by the BLR size-luminosity relation of Kaspi et al. (2000, see their Eq. 6). (14) The time lag measured in this work using broadband light curves.

(a) Highlighted table rows indicate objects for which a statistically significant signal is detected (see §4.3).

(b) Values correspond to centroid observed-frame values (Kaspi et al. 2000, see their table 6).

(c) Data for H α are not available. Time lag corresponds to the H β line.

Having gained some understanding of the advantages and limitations of broadband photometric reverberation mapping, we now wish to test the method using real data. Unlike the models described in §3, real data are often characterized by uneven sampling, gaps, and a varying signal to noise across the light curve. Here we consider a subset of the Palomar-Green (PG) sample of objects¹² (Schmidt & Green 1983), for which Johnson-Cousins B and R photometry is publicly available¹³ (Maoz et al. 1994; Giveon et al. 1999), and independent BLR size measurements are available through spectroscopic reverberation mapping (Kaspi et al. 2000). The properties of the sample are given in table 1.

While the PG sample provides a natural testbed for our purpose, it is far from being ideal: the typical number of points per light curve is small, ~ 50 , and the photometric errors non-negligible, $\lesssim 2\%$ (c.f. Fig. 7). Other photometric data sets are, in principle, available (Geha et al. 2003; Meusinger et al. 2011) but do not yet have BLR size measurements with which our findings may be compared [see Chelouche et al. (2011)].

4.1. Preliminaries

We first identify line-rich and line-poor bands given the typical quasar spectrum (Vanden Berk et al. 2001), the spectroscopically-determined redshift for the PG sample (Kaspi et al. 2000), and the relevant filter throughput curves (Fig. 11). In particular, we need to identify the filter with the larger relative contribution of emission lines to the variance

of the light curve. This is, however, difficult to estimate, since the variability properties of only a few lines, in only a few objects, are sufficiently well understood. Instead, we adopt a simplified approach and *assume* that the contribution of emission lines to the variance is proportional to their relative contribution to the flux. This is a fair approximation if, for example, the relative flux variations in all emission lines are comparable. This is supported by theory (Kaspi & Netzer 1999) and by the fact that the fractional variability of the Balmer lines is independent of their flux (Kaspi et al. 2000, see their table 5).

To properly account for the contribution of emission lines to the flux in some band, spectral decomposition of all prominent line, line blends, and continuum emission processes is required. To this end, we considered the high signal-to-noise (S/N) composite quasar spectrum of Vanden Berk et al. (2001), and identified all prominent emission lines and blends in the relevant wavebands. To fit for continuum emission, we identified line-free regions over the entire spectral range from rest-UV to the optical (Kaspi et al. 2000; Vanden Berk et al. 2001), and fitted a double powerlaw model (see Fig. 11), which accounts for the changing slope at optical wavelengths. The stronger Balmer emission lines were fitted with a two Gaussian model, which accounts for their relatively narrow line cores and extended wings. Weaker lines were fitted with a single Gaussian model. Iron blend emission templates, as derived for IZw I (Véron-Cetty et al. 2004; Vestergaard & Wilkes 2001), were convolved with a Gaussian kernel and fitted to the data. Independently adjusting the width and normalization for each Gaussian kernel (individual lines and blends), a reasonable agreement was sought. We model the Balmer continuum using the analytic expression of Grandi (1982). We emphasize that our model is by no means

¹² We choose to not focus our attention on active galactic nuclei (i.e., low luminosity quasars) since, in this case, great care is needed to make sure that varying seeing conditions do not introduce additional noise whose characteristics are poorly understood. In this case, specific data reduction techniques, such as aperture photometry, may be of advantage.

¹³ <http://wise-obs.tau.ac.il/PG.html>

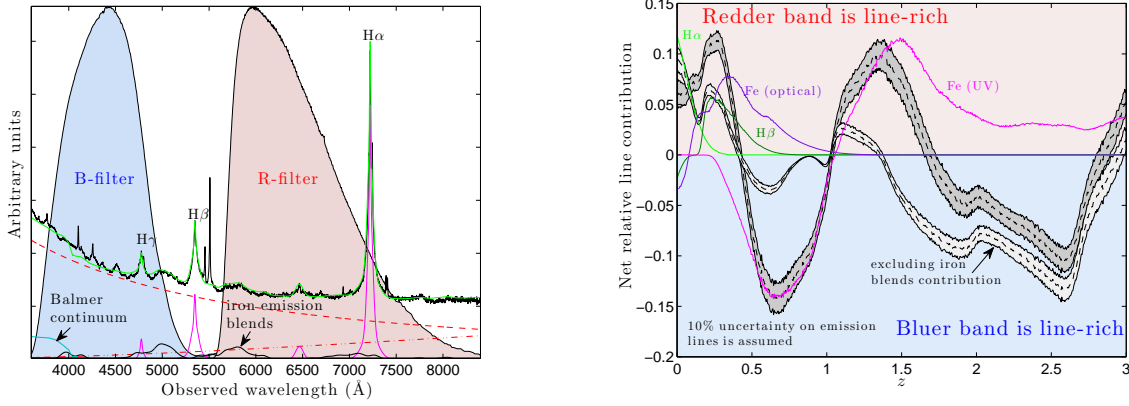


Figure 11. Emission line and continuum contribution to the Johnson-Cousins broadband filters. *Left:* the composite quasar spectrum (Vanden Berk et al. 2001, assumed to be at $z = 0.1$; see table 1) is shown together with the B - and R -filter response functions. Spectral decomposition into prominent emission lines (magenta) and iron line blends (gray curve) is shown. A double powerlaw continuum emission model is also included (dashed and dash-dotted magenta lines), and the “best-fit” model is shown in green. *Right:* the net emission line contribution to the broadband light curves as a function of the quasar redshift (dashed black lines; gray hatched patterns indicate the uncertainties assuming a 10% uncertainty on the flux of individual lines). The net contribution of a few particular lines is shown in colored curves. The sum of all lines excluding iron (light grey) and including iron (dark grey) are shown, indicating that in either case the R -filter is relatively line-rich for $z < 0.1$ objects with the Balmer emission line contribution being the dominant one. Typical redshift intervals over which line-rich filter identifications change are greater than the typical uncertainty associated with photometric redshifts (Weinstein et al. 2004; Wu & Jia 2010).

physical, nor uniquely-determined, and that its sole purpose is to allow for the qualitative estimate of the emission line contribution to the flux in each band. The decomposed spectrum is shown in figure 11.

The line-rich band, as a function of the quasar redshift, for the Johnson-Cousins filter scheme, is shown in figure 11. Clearly, depending on the object’s redshift, either the B or the R filter may be identified with the line-rich band. Typically, a redshift accuracy of 0.2 is required to securely identify the line-rich band, which is within reach of photometric redshift determination techniques (Richards et al. 2001). We find that, for $z < 0.5$ quasars, the R band may be identified with the line-rich band (i.e., with the Y -band, using the nomenclature of §2.1.2). This result is rather insensitive to whether or not the optical iron blends contribute to the variance on the relevant timescales. For $z < 0.25$ objects, the flux and, by assumption, the variance, are largely dominated by the Balmer lines. Uncertainties of order 10% in the flux of individual lines and line blends do not significantly change this result.

4.2. Methods

Aiming to analyze individual objects in the PG sample having a marginally adequate number of points in their light curves (thereby resulting in a large uncertainty on the determined lag; Fig. 7), we outline the formalism used below to assess the significance of our results.

4.2.1. Cross-correlation analysis

In analyzing real data for individual objects in the PG sample (table 1), it is important to verify that the detected signal is real and is not some artifact of non-even sampling or the particular light curve observed. There are several methods in the literature for cross-correlating realistic data sets: the interpolated cross-correlation function (Gaskell & Sparke 1986, ICCF; used in §3) and the discrete correlation function (Edelson & Krolik 1988, DCF). While the ICCF may be somewhat more sensitive to low-level signals, it is also more prone to sampling artifacts (Peterson 1993). To verify the significance of the ICCF signal, two algorithms are often used to estimate the uncertainty in the deduced correlation function: the flux randomization (FR) and the random subset selection

(RSS). In a nutshell, the first algorithm adds noise according to the measurement errors, and repeats the analysis many times to estimate the uncertainty associated with the results, while the latter method resamples the light curves (while losing $\sim 37\%$ of the data), to reach the same goal. Quite often both tests are combined to form the FR-RSS method, which is our method of choice in the present analysis. When considering the DCF approach, the z -transformed DCF algorithm (ZDCF) by Alexander (1997) often produces the best results, and is the approach adopted here. While all the aforementioned algorithms have been thoroughly tested with respect to spectroscopic reverberation mapping, their adequacy for the photometric reverberation mapping method is yet to be examined.

Our implementation of the ICCF (FR and RSS algorithms alike) is standard (Peterson et al. 1998). Nevertheless, because photometric reverberation mapping requires the subtraction of two cross-correlation functions, and to avoid interpolations of any kind¹⁴, our implementation of the ZDCF algorithm requires that both the $f_Y * f_X$ and $f_X * f_X$ terms in equation 5 are evaluated over an identical time grid, and that the bin center is identified with the time tag for that bin, i.e. δt . Similar considerations apply also when evaluating ξ_{AA} . Furthermore, we require that the number of independent pairs contributing to each bin in the correlation functions is ≥ 11 (Alexander 1997). For simplicity, we use equally spaced bins to evaluate ξ_{CA} and ξ_{AA} , and repeat the analysis many times by randomly selecting independent pairs (Alexander 1997). This provides us with a distribution of ξ_{CA} and ξ_{AA} values at each time bin, from which the mean and its uncertainty (associated with one standard deviation) are evaluated.

Spectroscopic reverberation mapping often employs two distinct approaches to estimate the time lag: by measuring the position of the peak of the correlation function, or by measuring its centroid. While the results are comparable, they are not identical and many works have discussed the pros and cons associated with each approach (Kaspi et al. 2000, and

¹⁴ Although we do not use this method here, we note that due to the correlated nature of the correlation function, interpolation at the correlation function level is likely to provide results which are less sensitive to sampling artifacts than the ICCF method.

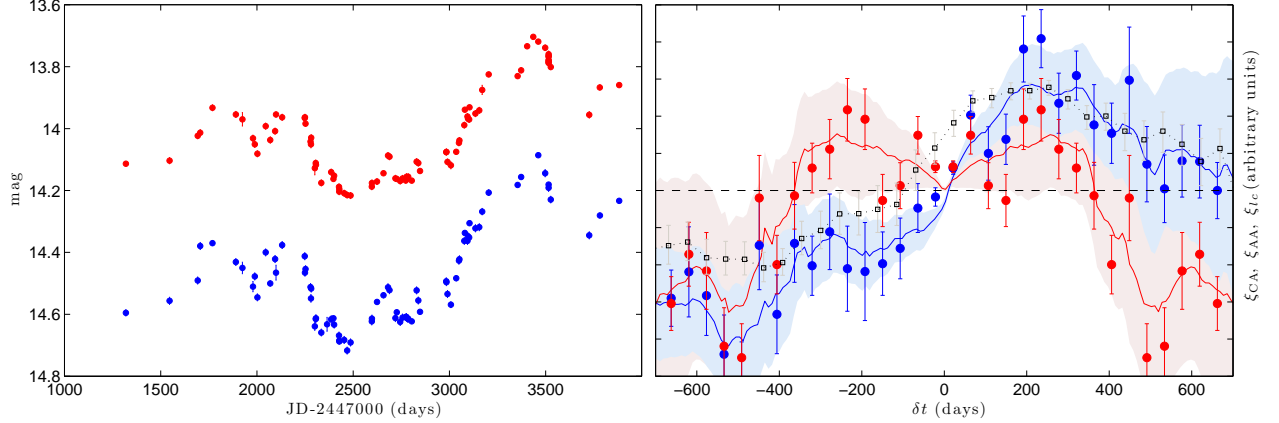


Figure 12. Light curve analysis for PG 0804+761. *Left:* The *B* and *R* light curves show significant non-monotonic variability over a few hundreds days timescales (see table 1). *Right:* the calculated statistical estimators, ξ_{CA} (blue shades) and ξ_{AA} (red shades). Also shown is the renormalized ξ_{IC} (black points) based on the spectroscopic data of Kaspi et al. (2000). Two analysis methods are used to calculate the photometric estimators: ICCF (solid lines and shades) and ZDCF (discrete points), which lead to consistent results. The uncertainty on each estimator was calculated using 100 Monte Carlo simulations: the FR-RSS method was used to estimate the error on the ICCF, and a random independent pair selection was used to estimate the error on the ZDCF (see text). All estimators peak at $\delta t \simeq 200$ days. The result obtained using ξ_{CA} has a higher statistical significance, and both photometric estimators are less significant than the spectroscopic one.

references therein). Similar algorithms are implemented here.

Estimating the uncertainty on the measured time-lag is done in the following way: we use the set of Monte Carlo simulations described above and calculate ξ_{CA} , ξ_{AA} for each realization. The time-lag is identified either with the peak or with the centroid of the statistical estimators¹⁵, and a distribution of time-lags is obtained. The uncertainty on the time-lag is associated with one standard deviation of that distribution.

4.2.2. Controlling systematics

In addition to the above algorithms, aimed at testing the robustness of the signal, we provide an additional test to identify systematic effects of the type discussed in §3.2.5 and to assist in screening against problematic data sets that may lead to spurious signals. To this end we use the bootstrapping method discussed in §3.2.5, verifying that the mean contribution of the simulated emission line to the flux of the line-rich band is that given in Fig. 11, and that the variance of the line light curve is consistent with the Kaspi et al. (2000, see their table 5) results.

4.3. Results

Here we outline the results for individual objects enlisted in table 1: we first discuss quasars for which a significant signal is detected¹⁶, and then cases where the analysis does not result in a discernible peak in either estimator. Our treatment of the ensemble as a whole is given in §4.3.9.

4.3.1. PG 0804+761

The *B* and *R* light curves for PG 0804+761 (henceforth termed PG 0804), at $z = 0.1$, are shown in figure 12 where large non-monotonic flux variations are evident. This object has the best sampled light curves in the Kaspi et al. (2000) sample, with a mean uncertainty on the flux measurement

¹⁵ Here we use the smoothing algorithm defined in §3.1, to avoid identifying spurious peaks with the physically meaningful peak.

¹⁶ The significance criterion used here requires a $\gtrsim 1\sigma$ signal (with σ being the one standard deviation uncertainty on the measured value) detected in both statistical estimators, and for which the ICCF and ZDCF analysis yield consistent results.

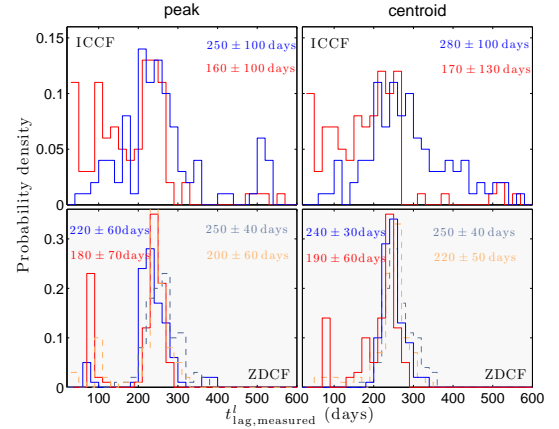


Figure 13. The peak (left panels) and centroid (right panels) $t_{lag,measured}^I$ distributions for PG 0804, obtained using sets of 100 Monte Carlo simulations (standard color scheme is used). ICCF (ZDCF) results are shown in the upper (lower) panels. When using the ZDCF approach, two different bin sizes were assumed (solid and dashed lines; red/blue shades correspond to ξ_{AA}/ξ_{CA}), and consistent results are obtained in both cases. The mean lag and its uncertainty (assumed to be one standard deviation) corresponding to each distribution are denoted in each panel. Centroid statistics results in slightly larger time-lags due to the non-symmetric shape of the statistical estimators around the peak (Fig. 3). While the time-lags inferred by all statistical estimators and methods are statistically consistent, the uncertainties inferred by the ZDCF approach are relatively small, and possibly less reliable (see text).

in both bands being of order 1% (with maximum uncertainties on individual measurements being $\sim 2\%$). The normalized variability measure is among the largest in the sample $\sim 17\%/14\%$ for the *B*/*R* bands (Table 1). As such, it is a promising candidate for photometric reverberation mapping.

Figure 11 indicates that, at its redshift, the *R* band is relatively line-rich (the net contribution of the lines to the bands is $\sim 6\%$), with $H\alpha$ being the dominant emission line. We calculated ξ_{CA} and ξ_{AA} using the ICCF and ZDCF algorithms. Unsurprisingly, the ZDCF method is somewhat more noisy than the ICCF methods (Kaspi et al. 2000, see their Fig. 4). That said, we find the results of all methods of analyses to be consistent given the uncertainties. This means that interpolation is not a major source of uncertainty for this object, which is consistent with the relative regular sampling of its light curves.

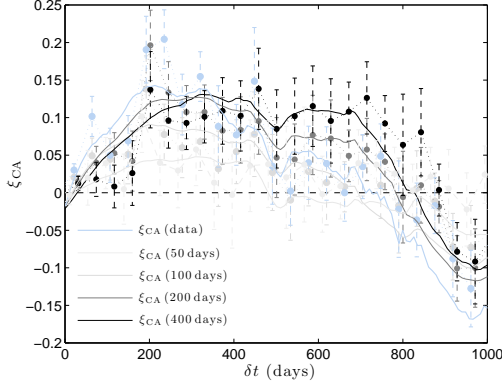


Figure 14. Photometric analysis of real B data and simulated R data for PG 0804. Several artificial time-lags (see legend) are assumed and the line-rich R band light curve is simulated using the line-poor B -band light curve (see §4.2.2). Analysis results for the real data are shown, for comparison, in blue shades. Both ICCF and ZDCF results are shown. Different artificial time-lags result in statistically different signals. As expected, longer time-lags result in a hump extending to longer timescales. The current data set is insensitive to short lags due to inadequate cadence. Qualitatively, an input time lag of 100-200 days is consistent with the observed signal.

Our analysis shows the expected features: a hump in both ξ_{CA} and ξ_{AA} , which peaks at similar ($\delta t \sim 200$ days) timescales. For comparison, we used a published light curve for the broad H α emission line (Kaspi et al. 2000)¹⁷, and calculated ξ_{lc} using the ZDCF algorithm. Clearly, both statistical estimators defined here trace the line-to-continuum cross-correlation function with a varying degree of significance: ξ_{CA} shows a $\gtrsim 2\sigma$ peak (σ being the uncertainty around the maximum), while the peak in ξ_{AA} is only $\gtrsim 1\sigma$ significant.

Using the Monte Carlo simulations described in §4.2.1, peak or centroid time distributions were obtained, and are shown in figure 13. Clearly, time-lag estimates qualitatively agree between the different methods. Quantitatively, however, there are some differences: the centroid method results in somewhat larger values for the time-lag. This results from the non-symmetric nature of ξ_{CA} , ξ_{AA} showing a more extended wing toward longer time-delays (Fig. 12). Results based on the ZDCF approach result in errors, which are typically smaller than those obtained using the ICCF method. This results from the fact that the ZDCF peak is largely determined by a few individual bins (note the two bins around 200 days that lie above most other ZDCF points, as well as above the ICCF curve; Fig. 12). In fact, the resulting uncertainty on the ZDCF, being of order 20% in this case, is smaller than predicted based on our Monte Carlo simulations presented in figure 7. We conclude that estimating the uncertainty on the time-lag using the ZDCF results may be less reliable.

Using the ICCF time-lag distributions, we determine the observed time-lag for PG 0804 to be 250 ± 100 days, which is statistically consistent with the spectroscopically measured value of 193^{+20}_{-17} days (Kaspi et al. 2000). As far as systematics is concerned, we do not expect a bias in the measured lag to exceed $\sim 40\%$ given that $t_{\text{tot}}/t_{\text{lag,measured}}^l \gtrsim 10$ (Fig. 10).

Using the numerical bootstrapping scheme defined in §4.2.2, we find that an input time lag of 100 – 200 days is qualitatively consistent with the data. In particular, much shorter or much longer time-lags, are inconsistent with our findings in

terms of signal amplitude and shape. Interestingly, a weak yet marginally significant hump at around 200 – 300 days is implied by the data even when much shorter artificial time-lags are used as input. Therefore, one should be careful when interpreting marginally significant signals. For the specific case considered here we can conclude that the data cannot be used to detect short time-lags, which is of no surprise given that the cadence of the light curves is at 20 – 30 days intervals.

To conclude, the time-lag estimated here by the photometric reverberation mapping approach is $\simeq 200 \pm 100$ days, and is therefore consistent with the value deduced by Kaspi et al. (2000), albeit with an expectedly larger uncertainty.

4.3.2. PG 0844+349

This low- z , low-luminosity object has a potentially prominent ($\sim 8\%$) line contribution to the R -band from the Balmer emission lines. With $\lesssim 70$ points in its light curve, and what appears to be significant variations over 200 days time scales, our analysis reveals a marginal ($\gtrsim 1\sigma$ using the FR-RSS method and $\gtrsim 2$ using ZDCF statistics) peak at ~ 500 days (Fig. 15). The spectroscopically measured time-lag for this object is of order 50 days and agrees with the value expected from the BLR size vs. luminosity relation (table 1). Nevertheless, the data do not show a corresponding peak at those time-scales. In fact, our simulations indicate that only a time-lag $\gtrsim 100$ days, could have been detected with some certainty. Interestingly, simulations with an input lag of 500 days (§4.2.2) are able to qualitatively account for the observed signal (dashed magenta curve in figure 15).

It is not clear whether a 500 days lag, *if* real, is associated with a long-term reverberation signal of the BLR, since there is no corresponding signal in the Kaspi et al. (2000) analysis of the spectroscopic data. We note, however, that it is also possible that the measurement uncertainties are somewhat under-estimated for this object, hence the significance of our deduced signal over-estimated. That this might be the case is hinted by the normalized variability measure in both the B and R bands being similar (contrary to naive theoretical expectations) and the fact that contamination by the host galaxy in this low- z quasar may be important (see below).

4.3.3. PG 1229+204

This quasar, being at low redshift ($z = 0.064$) has one of the most prominent ($\lesssim 8\%$) Balmer line contributions to the R -band among the PG objects in our sample. The analysis detects a significant *trough* at $\gtrsim 200$ days, in both statistical estimators, and using both the ICCF and the ZDCF methods. This is unexpected since a peak rather than a trough is predicted by the simulations for an expected lag of ~ 34 days (Fig. 15). Simulating cases with time-lags of order 200 days also produces a peak, in contrast to the observed signal. The interpretation that the B - rather than the R -band is the line-rich band, is not supported by the optical spectrum showing rather typical quasar emission lines (Kaspi et al. 2000).

We cannot positively identify the origin of the unexpected signal but note that, at its low redshift, and being a rather faint low-luminosity quasar, the host galaxy is likely to substantially contribute to the flux in the bands. This has a dual result: 1) the actual contribution of the emission lines to the bands is smaller than that predicted here, and 2) the data may be substantially affected by varying seeing conditions between the nights, thereby contributing to the variance in the light curves, and masking the true signal. Interestingly, the reduced variability measure in both bands is similar for this object, which

¹⁷ see <http://wise-obs.tau.ac.il/~shai/PG/>

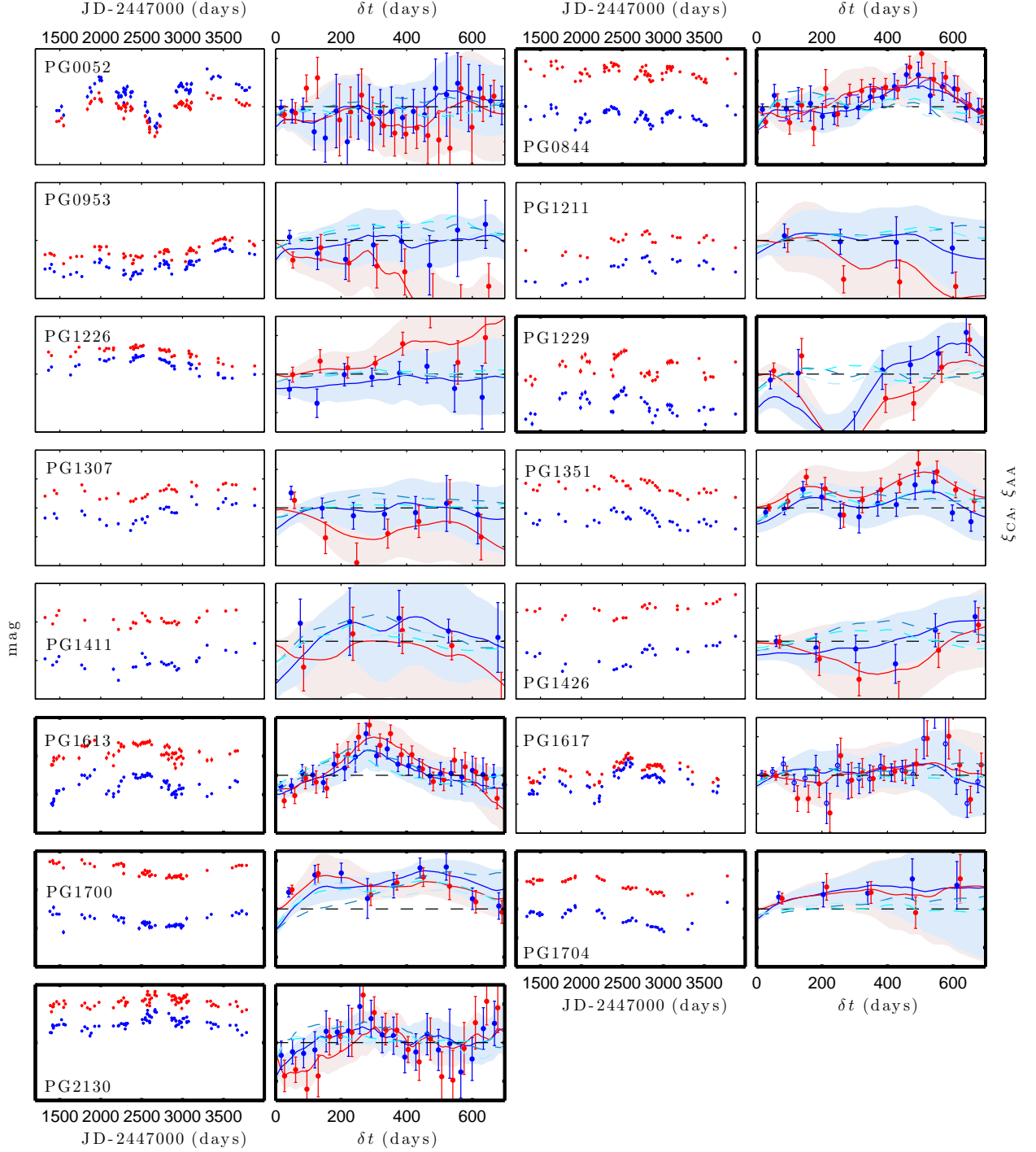


Figure 15. Analysis of 15 PG quasars from the sample of Kaspi et al. (2000, see our table 1). In each pair of columns, the left panel shows the B (blue points) and R (red points) light curves, and the right panel the calculated ξ_{CA} (blue curves and shades) and ξ_{AA} (red curves and shades) using the ICCF (solid lines) and ZDCF (points with error-bars) numerical schemes. Cases for which a statistically significant signal is detected in both estimators and using both numerical schemes, are highlighted. For each quasar, the results of three ξ_{CA} simulations are shown (in dashed blue-shaded curves) based on the expected time-lag from the BLR size vs. luminosity relation, $t_{lag,ex}^l$ (table 1): light to dark shades correspond simulated time-lags of $t_{lag,ex}^l/2 \rightarrow t_{lag,ex}^l \rightarrow 2t_{lag,ex}^l$ (cyan curves correspond to $t_{lag,ex}^l$). For PG 0844, a simulation with a 500 days lag is also included (dashed magenta line). The ICCF results reported here are used to construct the ensemble averages considered in figure 17.

may indicate the presence of an additional source of noise not accounted for by the reported measurement uncertainties.

4.3.4. PG 1613+658

Analyzing the data for this object, a marginally significant signal (at the $1\sigma - 2\sigma$ level) is detected in both statistical estimators, at $\lesssim 300$ days (Fig. 15). Formally, ξ_{CA} statistics implies that the time lag is 300 ± 130 days. At its redshift, the net contribution of emission lines is of order 5%, and is therefore larger than the typical flux measurement uncertainty in this object ($\lesssim 2\%$). Simulations with an artificial lag of ~ 300 days are able to qualitatively account for the observed signal. Much shorter time lags [e.g., ~ 40 days, as spectroscopically deduced by Kaspi et al. (2000)] do not seem to be supported by our findings. Interestingly, for this object, spectroscopic time-lag measurements using the peak distribution function give very large errors for the $H\alpha$ line, and given its luminosity, PG 1613+658 lies considerably below the BLR size vs. luminosity relation (Kaspi et al. 2000, see also our table 1). Using our deduced lag, a better agreement is obtained with the Kaspi et al. (2000) size-luminosity relation.

4.3.5. PG 1700+518

This object shows a statistically significant ($2\sigma - 3\sigma$), wide peak extending over the range 150-450 days. Assuming that $H\beta$ is the main line contributor to the R band's flux, our simulations indicate that the signal is consistent with a time-lag of ~ 430 days (formally, ξ_{CA} statistics yields a 300 ± 160 days' lag). This value is statistically consistent with the time-delay measurement of Kaspi et al. (2000), but our deduced lag is in somewhat better agreement with the expected BLR size given the source luminosity (table 1). Our simulations show that time-lags considerably shorter ($\ll 200$ days) or longer ($\gg 800$ days) are less favored by the data and cannot fully account for the observed signal (Fig. 15).

4.3.6. PG 1704+608

This object, having ~ 40 visits in each band, shows a marginal ($\gtrsim 1\sigma$) hump at 200-300 days. Formally, the deduced time-lag is 400 ± 200 days, and is consistent with the values of Kaspi et al. (2000). At $z = 0.371$, the net contribution of emission lines to the line-rich R -band is only about twice as large as the mean measurement uncertainty. This, and the small number of data points, account for the low-significance of the observed signal. Further, simulations show that a marginal signal is indeed expected to occur at roughly the spectroscopically determined lag.

4.3.7. PG 2130+099

There is a hint for a localized ($\sim 1\sigma$) peak around 200-300 days in both statistical estimators (ξ_{CA} statistics yields a lag of 240 ± 100 days) using both the ICCF and the ZDCF methods. At face value, this timescale is consistent with the results of Kaspi et al. (2000) who find a time lag of ~ 200 days. Nevertheless, as discussed by Grier et al. (2008), the cadence of the Kaspi et al. (2000) observations may not be adequate to uncover the true time lag in this object. Specifically, Grier et al. (2008) find a time lag of order 30 days using better sampled light curves on short time scales. The fact that we do not find a significant peak on short timescales is not surprising since we are essentially using the Kaspi et al. (2000) data set.

4.3.8. PG 0026+129 and other objects yielding null results

Like PG 0804, PG 0026+129 ($z = 0.142$) is among the best-sampled quasars in our sample with ~ 70 points per light curve (see Fig. 16). While the normalized variability measure is comparable to that of PG 0804, most of the power is associated with long-term variability. In particular, when subtracting a linear trend from the light curve, the normalized variability measure drops by a factor of ~ 2 in both bands. At its redshift, the R -band is the line-rich (Fig. 11) with a net relative line contribution of $\sim 3\%$ due to $H\alpha$ (or $\sim 7\%$ if iron is important).

The statistical estimators calculated here do not yield a significant time-lag. Specifically, there is no discernible peak detected in either estimator using either cross-correlation method (i.e., ICCF or ZDCF). While de-trending seems to somewhat improve the signal (there is a 1σ hump at around 100 days), it falls short of revealing a significant result. We attribute our failure to securely identify a signal to a combination of factors related to the smaller variability measure on the relevant BLR-size timescales, as well as to the lower net contribution of emission lines to the filters, compared to the case of PG 0804.

PG 0052+251 has 72 points in each band, and a normalized variability measure of 26%/20% in the B/R bands, partly due to a sharp feature extending over ~ 200 days scales. The typical measurement uncertainty is $\lesssim 3\%$ in both bands. At $z = 0.155$, the net line contribution is of order 4%. i.e., comparable to the noise-level. Therefore, despite the relatively large number of visits, no clear signal is detected, in either statistical estimator, using either numerical scheme.

The remaining quasars in the Kaspi et al. (2000) PG sample also do not yield a significant signal. This is however expected given the small number of points in the photometric light curve of these quasars being ~ 40 (see Fig. 7). The fact that such objects do have a spectroscopically-determined time lag is also not surprising: the photometric approach to reverberation mapping is less sensitive than the spectroscopic one.

4.3.9. Ensemble averages

To overcome the limitations plaguing the analysis of individual objects, ensemble averages may be considered. As demonstrated in §3, combining the results for many objects, allows the time-lag to be determined with good accuracy, and was a main motivation on our part to develop this approach to reverberation mapping. Clearly, large ensembles are required to reach a robust result when less than favorable light curves are available on an individual case basis. Nevertheless, with upcoming photometric surveys, statistics is unlikely to be a limiting factor, and defining ensemble averages over narrow luminosity and redshift bins will be possible.

As our small sample of 17 PG quasars consists of a range of redshifts and quasar luminosities, we use the following transformation to put the results for different objects on an equal footing: $\delta t \rightarrow \delta t / [(1+z)L_{45}^\gamma]$, where $L_{45} \equiv \lambda L_\lambda (5100 \text{ \AA}) / 10^{45} \text{ erg s}^{-1}$. This transformation corrects for both cosmological time-dilation, and the fact that the BLR size scales roughly as L^γ . Following Kaspi et al. (2000), we take $\gamma = 0.7$ but note that similar results are obtained for $0.5 \lesssim \gamma \lesssim 0.7$ (Bentz et al. 2009, and references therein). Using the above transformation, all PG quasars are effectively transformed to a $z = 0$ quasar with $L_{45} = 1$.

Figure 17 shows the ensemble-averaged results for

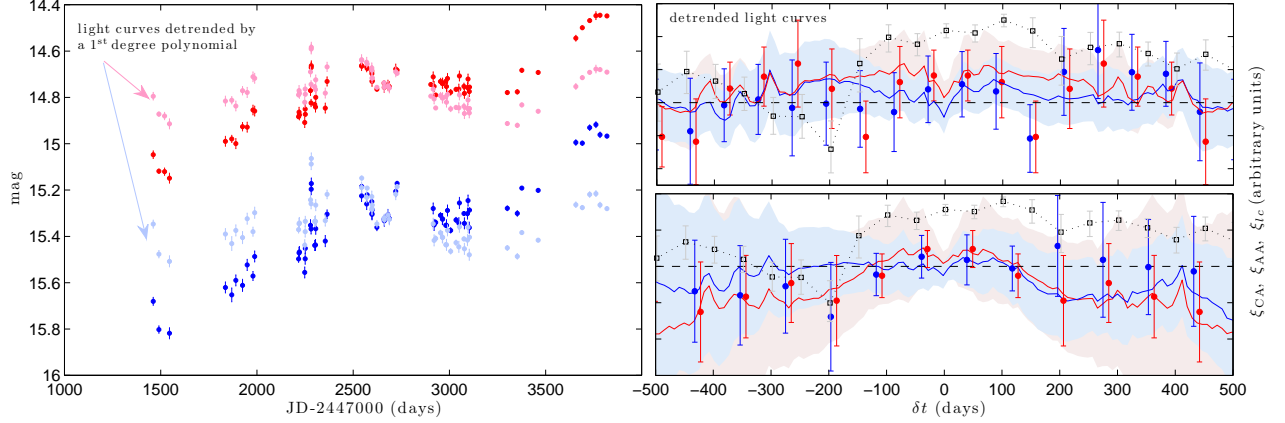


Figure 16. Light curve analysis for PG 0026+129. *Left:* The *B* and *R* light curves show significant variability on timescales of the order the duration of the light curve. De-trended light curves were calculated by subtracting a 1st-degree polynomial. The normalized variability measure for the de-trended light curves is a factor two smaller than the original data. *Right:* the calculated statistical estimators for the de-trended light curves (upper panel) and the original data (lower panel). See the caption of figure 12 for the meaning of different curves. While de-trending seems to be able to improve the signal, a statistically significant peak is not detected by either method.

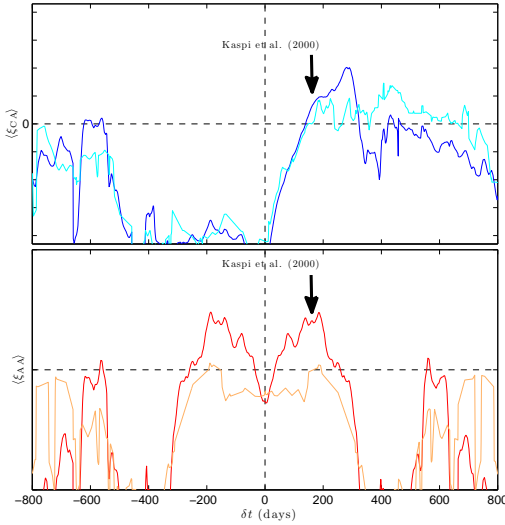


Figure 17. Ensemble averages for ξ_{CA} (upper panel) and ξ_{AA} (lower panel), for the PG sample of 17 quasars from Kaspi et al. (2000, see our table 1). Both the arithmetic mean (dark shades) and the median (light shades) are shown. Ensemble averages for both statistical estimators give consistent results, and peak around 180-280 days. This is in agreement with the predicted time-lag based on the BLR size vs. luminosity relation of Kaspi et al. (2000), for a typical $L_{45} = 1$ quasar (see text). The median shows a less significant peak although the results are qualitatively consistent with the ensemble mean. This demonstrates the feasibility of the photometric reverberation mapping technique in uncovering the typical time-lag in an ensemble of objects for which individual time-lag determination is difficult to achieve.

ξ_{CA} , ξ_{AA} for the entire PG sample (table 1). We deliberately include all objects regardless of data quality issues (as in the case of e.g., PG 1229). A peak in both (mean) statistical estimators is seen around 200 days. This value is similar to a time-lag of 170 days, which is the value predicted by the Kaspi et al. (2000) BLR size-luminosity relation for a $L_{45} = 1$ quasar. Also plotted are the median results for both statistical estimators. Both the mean and the median provide qualitatively consistent results, although quantitative differences do exist. Given the small nature of the sample, we do not present estimates for the uncertainty on the mean/median values.

To conclude, averaging the results for the PG quasar sample, we obtain a similar peak in both statistical estimators,

occurring at times which are qualitatively consistent with the BLR sizes implied by the Kaspi et al. (2000) results. A larger sample of objects will allow to better quantify the mean time lag for sub-samples of quasars over narrow luminosity and redshift intervals. Alternatively, better quality data (higher S/N, and better sampled light curves) could be used to better constrain the time-lag for individual objects in the PG sample of quasars.

5. SUMMARY

We demonstrated that line-to-continuum time-delays associated with the broad emission line region in quasars can be deduced from broadband photometric light curves. This is made possible by defining appropriate statistical estimators [termed $\xi_{CA}(\delta t)$ and $\xi_{AA}(\delta t)$] to process the data, and which effectively subtract the continuum contribution to the cross-correlation signal of the light curves. Using this formalism, the time-lag is identified with the time δt at which these estimators peak.

The proposed formalism makes use of the fact that line and continuum processes have very different variability properties, and that quasars exhibit large amplitude variations on timescales comparable to the BLR light crossing time. The formalism is generally adequate for cases in which few strong emission lines, having different intensities, contribute to the spectrum, as indeed characterizes the optical emission spectrum of quasars.

To effectively apply the method, prior knowledge of the quasar redshift (using either photometric or spectroscopic means) is required to identify relatively line-dominated and line-free spectral bands. Together with knowledge of the filter response functions, these may be used to better implement the algorithm and interpret the results. Using numerical simulations, we demonstrated that photometric reverberation mapping is feasible under realistic observing conditions and for typical quasar properties. We showed, by means of numerical simulations and real data (pertaining to the PG quasar sample), that the measurement of the line-to-continuum time-delay is robust although somewhat less accurate than that obtained using the spectroscopic reverberation mapping technique. In addition, we quantify biases in the photometrically deduced time-lags, which are sensitive to the BLR geometry and the duration of the light curve. We identify their origin

and suggest several methods to correct for them. In addition, we qualitatively study potential biases associated with the presence of multiple emission lines in quasar spectra, and with finite inter-band continuum time-delays.

The main advantage of the photometric approach to reverberation mapping over other methods is that it is *considerably* more efficient and cheap to implement, and can therefore be applied to large samples of objects. In fact, any survey which photometrically monitors the sky with proper cadence and signal-to-noise in two or more filters, and for which quasars may be identified and their redshift estimated, can be used to measure the size of the BLR. We demonstrated that, with large enough samples of quasars, it is possible to beat down the noise, and deduce (statistical) BLR size measurements that are considerably more accurate than are currently achievable by spectroscopic means.

By combining photometric light curves with single epoch spectroscopic measurements, which allow to estimate the velocity dispersion of the BLR, it may be possible to measure the black hole mass in orders of magnitude more objects than are directly measurable by other means. This would allow for the statistical measurement of the SMBH mass for sub-samples of quasars (selected according to e.g., their luminosity, redshift, or colors), leading to highly accurate results, and potentially revealing differences between different classes of objects, which, thus far, may have eluded detection.

To conclude, photometric surveys that monitor the sky on a regular basis are likely to play a major role in the coming decades in the (statistical) measurement of the BLR size in quasars, as well as in determining their black hole masses. This will lead to a more complete census of black holes over cosmic time, and shed light on outstanding problems concerning the formation and co-evolution of black holes and their host galaxies.

We thank E. Behar, T. Holczer, and S. Kaspi for thought-provoking weekly meetings that triggered much of this work, and the referee for insightful comments. D. C. thanks C. Kochanek, D. Maoz, and H. Netzer for valuable comments on an earlier version of this paper, and S. Kaspi, A. Laor, H. Netzer, and C. Thompson for wise advice. Fruitful discussions with D. V. Bowen, D. Dultzin, K. Horne, Y. Krongold, S. Rafter, and O. Shemmer are greatly appreciated. We thank M. Vestergaard for providing us with iron UV emission templates. This research has been supported in part by a FP7/IRG PIRG-GA-2009-256434, and by grant 927/11 from the Israeli Science Foundation. E. D. thanks E. Behar for financial support. D. C. thanks Chuli and the people of Arlozorov café for continuous encouragement.

REFERENCES

- Alexander, T. 1997, *Astronomical Time Series*, 218, 163
 Bachev, R. S. 2009, *A&A*, 493, 907
 Bahcall, J. N., Kozlovsky, B.-Z., & Salpeter, E. E. 1972, *ApJ*, 171, 467
 Baldwin, J. A., & Netzer, H. 1978, *ApJ*, 226, 1
 Barth, A. J., Nguyen, M. L., Malkan, M. A., et al. 2011, *ApJ*, 732, 121
 Bentz, M. C., Peterson, B. M., Netzer, H., Pogge, R. W., & Vestergaard, M. 2009, *ApJ*, 697, 160
 Bentz, M. C., et al. 2010, *ApJ*, 720, L46
 Blandford, R. D., & McKee, C. F. 1982, *ApJ*, 255, 419
 Vanden Berk, D. E., et al. 2001, *AJ*, 122, 549
 Chelouche D., Daniel, E., Geha M. C., & Kaspi, S. 2011, *ApJ*, submitted
 Collier, S. J., et al. 1998, *ApJ*, 500, 162
 Collin, S., & Kawaguchi, T. 2004, *A&A*, 426, 797
 Czerny, B., Schwarzenberg-Czerny, A., & Loska, Z. 1999, *MNRAS*, 303, 148
 Dietrich, M., et al. 1993, *ApJ*, 408, 416
 Edelson, R. A., & Krolik, J. H. 1988, *ApJ*, 333, 646
 Ferrarese, L., Pogge, R. W., Peterson, B. M., Merritt, D., Wandel, A., & Joseph, C. L. 2001, *ApJ*, 555, L79
 Gaskell, C. M., & Peterson, B. M. 1987, *ApJS*, 65, 1
 Gaskell, C. M., & Sparke, L. S. 1986, *ApJ*, 305, 175
 Gebhardt, K., et al. 2000, *ApJ*, 539, L13
 Gebhardt, K., et al. 2000, *ApJ*, 543, L5
 Geha, M., et al. 2003, *AJ*, 125, 1
 Genzel, R., Eckart, A., Ott, T., & Eisenhauer, F. 1997, *MNRAS*, 291, 219
 Giveon, U., Maoz, D., Kaspi, S., Netzer, H., & Smith, P. S. 1999, *MNRAS*, 306, 637
 Goad, M. R., O'Brien, P. T., & Gondhalekar, P. M. 1993, *MNRAS*, 263, 149
 Grandi, S. A. 1982, *ApJ*, 255, 25
 Greene, J. E., & Ho, L. C. 2005, *ApJ*, 630, 122
 Greene, J. E., & Ho, L. C. 2006, *ApJ*, 641, L21
 Grier, C. J., et al. 2008, *ApJ*, 688, 837
 Hopkins, P. F., Robertson, B., Krause, E., Hernquist, L., & Cox, T. J. 2006, *ApJ*, 652, 107
 Horne, K., Peterson, B. M., Collier, S. J., & Netzer, H. 2004, *PASP*, 116, 465
 Kaspi, S., Brandt, W. N., Maoz, D., Netzer, H., Schneider, D. P., & Shemmer, O. 2007, *ApJ*, 659, 997
 Kaspi, S., Maoz, D., Netzer, H., Peterson, B. M., Vestergaard, M., & Jannuzi, B. T. 2005, *ApJ*, 629, 61
 Kaspi, S., & Netzer, H. 1999, *ApJ*, 524, 71
 Kaspi, S., Smith, P. S., Netzer, H., Maoz, D., Jannuzi, B. T., & Giveon, U. 2000, *ApJ*, 533, 631
 Kauffmann, G., & Haehnelt, M. 2000, *MNRAS*, 311, 576
 Kollatschny, W. 2003, *A&A*, 407, 461
 Kollmeier, J. A., et al. 2006, *ApJ*, 648, 128
 Koratkar, A. P., & Gaskell, C. M. 1991, *ApJ*, 370, L61
 Korista, K. T., et al. 1995, *ApJS*, 97, 285
 Krolik, J. H., Horne, K., Kallman, T. R., Malkan, M. A., Edelson, R. A., & Kriss, G. A. 1991, *ApJ*, 371, 541
 Krolik, J. H. 2001, *ApJ*, 551, 72
 Lynden-Bell, D. 1969, *Nature*, 223, 690
 Magorrian, J., et al. 1998, *AJ*, 115, 2285
 Maoz, D., et al. 1991, *ApJ*, 367, 493
 Maoz, D., Smith, P. S., Jannuzi, B. T., Kaspi, S., & Netzer, H. 1994, *ApJ*, 421, 34
 McGill, K. L., Woo, J.-H., Treu, T., & Malkan, M. A. 2008, *ApJ*, 673, 703
 MacLeod, C. L., et al. 2010, *ApJ*, 721, 1014
 Meusinger, H., Hinze, A., & de Hoon, A. 2011, *A&A*, 525, A37
 Miyoshi, M., Moran, J., Herrnstein, J., Greenhill, L., Nakai, N., Diamond, P., & Inoue, M. 1995, *Nature*, 373, 127
 Netzer, H. 2003, *ApJ*, 583, L5
 Netzer, H., & Peterson, B. M. 1997, *Astronomical Time Series*, 218, 85
 Onken, C. A., & Peterson, B. M. 2002, *ApJ*, 572, 746
 Osmer, P. S. 2004, *Coevolution of Black Holes and Galaxies*, 324
 Pelupessy, F. I., Di Matteo, T., & Ciardi, B. 2007, *ApJ*, 665, 107
 Peterson, B. M. 1988, *PASP*, 100, 18
 Peterson, B. M. 1993, *PASP*, 105, 247
 Peterson, B. M. 2010, *IAU Symposium*, 267, 151
 Peterson, B. M., Bentz, M. C., Desroches, L.-B., et al. 2005, *ApJ*, 632, 799
 Peterson, B. M., et al. 2004, *ApJ*, 613, 682
 Peterson, B. M., & Wandel, A. 1999, *ApJ*, 521, L95
 Peterson, B. M., Wanders, I., Horne, K., Collier, S., Alexander, T., Kaspi, S., & Maoz, D. 1998, *PASP*, 110, 660
 Reichert, G. A., et al. 1994, *ApJ*, 425, 582
 Richards, G. T., Weinstein, M. A., Schneider, D. P., et al. 2001, *AJ*, 122, 1151
 Salpeter, E. E. 1964, *ApJ*, 140, 796
 Schmidt, M., & Green, R. F. 1983, *ApJ*, 269, 352
 Sergeev, S. G., Doroshenko, V. T., Golubinskiy, Y. V., Merkulova, N. I., & Sergeeva, E. A. 2005, *ApJ*, 622, 129
 Shakura, N. I., & Sunyaev, R. A. 1973, *A&A*, 24, 337
 Shields, G. A., Gebhardt, K., Salvander, S., Wills, B. J., Xie, B., Brotherton, M. S., Yuan, J., & Dietrich, M. 2003, *ApJ*, 583, 124
 Shields, G. A., Menezes, K. L., Massart, C. A., & Vanden Bout, P. 2006, *ApJ*, 641, 683
 Trakhtenbrot, B., & Netzer, H. 2010, *MNRAS*, 406, L35
 Véron-Cetty, M.-P., Joly, M., & Véron, P. 2004, *A&A*, 417, 515
 Vestergaard, M. 2002, *ApJ*, 571, 733
 Vestergaard, M., & Osmer, P. S. 2009, *ApJ*, 699, 800
 Vestergaard, M., & Wilkes, B. J. 2001, *ApJS*, 134, 1

- Wandel, A. 1999, *ApJ*, 519, L39
Wanders, I., et al. 1995, *ApJ*, 453, L87
Weinstein, M. A., et al. 2004, *ApJS*, 155, 243
Welsh, W. F. 1999, *PASP*, 111, 1347
Woo, J.-H., Treu, T., Malkan, M. A., & Blandford, R. D. 2008, *ApJ*, 681, 925
Wu, X.-B., & Jia, Z. 2010, *MNRAS*, 406, 1583
Zhang, X.-G., Dultzin, D., & Wang, T.-G. 2008, *MNRAS*, 385, 1087
Zu, Y., Kochanek, C. S., & Peterson, B. M. 2011, *ApJ*, 735, 80